Revised Manuscript (Clean, unmarked, FINAL version)

Click here to view linked References

https://dx.doi.org/10.1016/j.ijhydene.2022.04.001

This is the Pre-Published Version.

Modeling and analysis of water vapor dynamics in High-Temperature proton exchange membrane fuel cell coupling gas-crossover phenomena

Caizhi Zhang [1, #, *], Jun Zhang [1, #], Quanneng Liu [1], Lang Cai [1], Meng Ni [2] , Tao Zeng [3], Cheng Liang [4, *]

[1] School of Mechanical and Vehicle Engineering; The State Key Laboratory of Mechanical Transmissions; Chongqing Automotive Collaborative Innovation Centre, Chongqing University, Chongqing, China

[2] Department of Building and Real Estate, Research Insitute for Sustainable Urban Development (RISUD) and Research Institute for Smart Energy (RISE), The Hong Kong Polytechnic University, Hung Hom, Kowloon, Hong Kong, China

[3] Propulsion Research Institute of Chongqing Changan New Energy Vehicle Technology Co., Ltd, Chongqing, China

[4] Beijing New Energy Vehicle Technology Innovation Center Co., Ltd, Beijing Automotive Research Center Co., Ltd, Beijing, China;

(#, equal contribution; *, Corresponding authors at C.Z Zhang (czzhang@cqu.edu.cn), C. Liang (liangchenfcv@126.com))

Abstract

A 3-D numerical model coupling gas-crossover phenomena for high-temperature proton exchange membrane fuel cell (HT-PEMFC) is developed to investigate the water vapor behavior. After model validation, sensitivity analysis of the water vapor diffusion coefficient is carried out, which does not further affect the water vapor behavior, when the order of magnitude of diffusion coefficient is higher than $10^{-5}\,m^2/s$. It is also found that the water vapor transport flux decreases with increasing membrane thickness. However, the flux increases slightly with increasing the catalyst layer. In addition, Increasing the pressure and humidity on the anode side will cause water vapor to diffuse from the anode to the cathode, while increasing the current density or the pressure of cathode, the rate of water vapor transport from the cathode to the anode is enhanced. In the dead-end mode, the accumulation of water vapor at the anode outlet is the main cause for the reversible performance decline, which can be restored through reasonable purge strategies. This work contributes to improve the water management strategy of HT-PEMFC operating in dead-end mode.

© 2022. This manuscript version is made available under the CC-BY-NC-ND 4.0 license http://creativecommons.org/licenses/by-nc-nd/4.0/.

Keywords: HT-PEMFC; Water vapor transportation and distribution; Gas-crossover phenomena; Purge process

Graphical Abstract

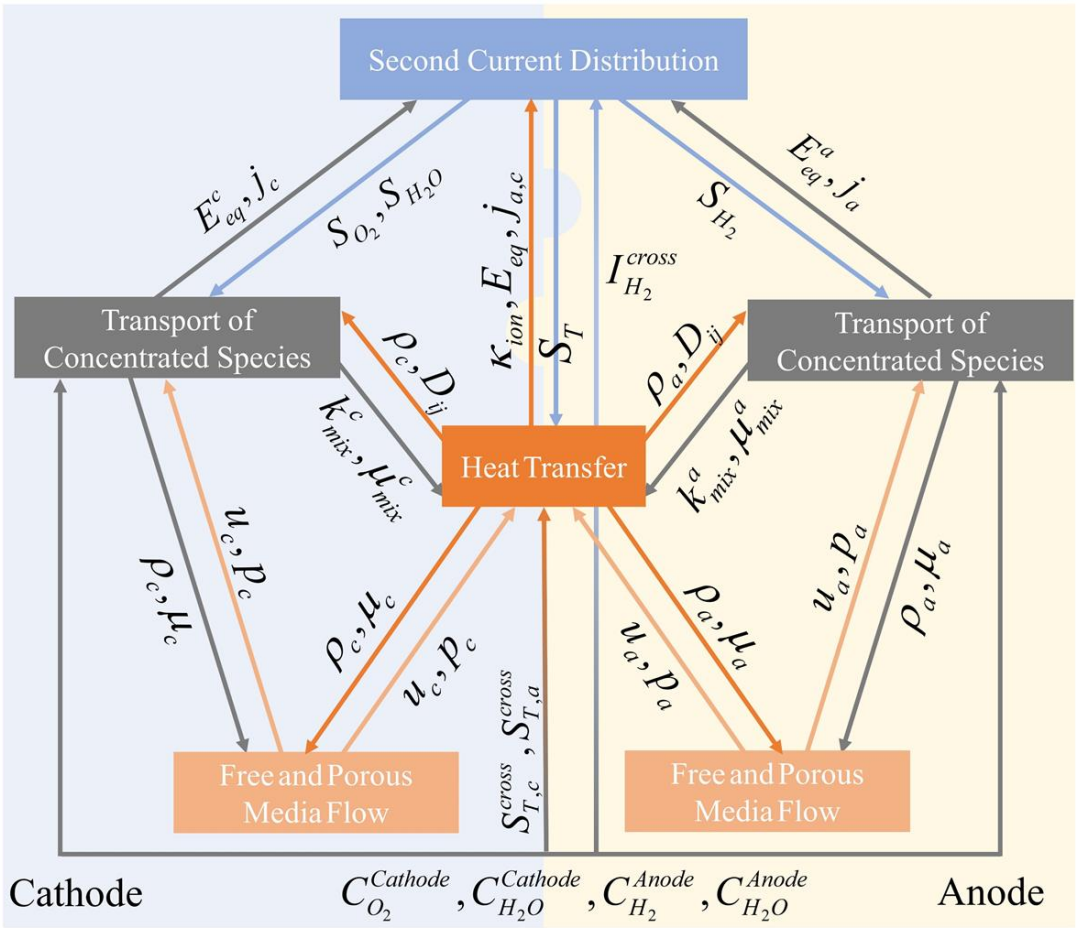

Nomenclature

A	area, m^2	t	thickness, m
$ECSA$	electrochemical surface area	μ	dynamic viscosity, kg/(m · s)
ACL	anode catalyst layer	x	mole fraction
BP	bipolar plate	η	overpotential, V
C	molar concentration, mol/m^3	χ	coefficient of thermal expansion, 1/K
CL	catalyst layer	ε	porosity
CCL	cathode catalyst layer	φ	phase potential, V
H	Henry's Law	ρ	density, kg/m^3
$\vec{d}$	diffusional driving force	α	transfer coefficient
C_p	specific heat capacity, J/(kg · K)	q	heat flux, W/m^2
D	diffusion coefficients, m^2/s	n	diffusion flux, $g/(m^2 \cdot s)$
DL	doping level of phosphoric acid in	θ	volume fraction of various substances in porous

	membrane		media
E_{MEM}	activation energy, J/mol	ω	mass fraction
E_{eq}	equilibrium potential, V	$\vec{u}$	velocity, m/s
GDL	gas diffusion layer	ν	Electrolyte volume fraction in CL
GC	gas flow channel	κ	Electrical/proton conductivity, S/m
K	permeability, m^2	ζ	stoichiometric ratio
$\vec{K}$	viscous stress tensor	∇	Hamiltonian operator
PA	Phosphoric Acid	**Subscripts and Superscripts**	
T	temperature, K	g	gas
M	molecular weight, g/mol	m	mass equation
MEM	membrane	u	momentum equation
S	source term	opt	operation
j	current density, A/cm^2	i,j	species index
J	volume current density, A/cm^3	ele	electronic
F	Faradays constant, 96487 C/mol	ion	ionic
R	universal gas constant, $8.3145 J/(K \cdot mol)$	in	inlet of gas channel
k	thermal conductivity, W/(m·K)	a,c	anode, cathode
p	pressure, Pa	$H_2, O_2,$	hydrogen, oxygen
P_{sat}	vapor saturation pressure, atm	eff	effective value in porous region
Δ	difference	ref	reference

1. Introduction

Proton exchange membrane fuel cells (PEMFCs) are economical and environmentally friendly power generation devices with high energy conversion efficiency and low emissions, which mainly use hydrogen and air as fuel and play an important role in the future "Hydrogen Economy" [1]. High-temperature proton exchange membrane fuel cells (HT-PEMFCs) with phosphoric acid-doped polybenzimidazole (PA-doped/PBI) membrane, which operates at higher than 100°C, have attracted a large interest in the fuel cell community all over the world since the concept of HT-PEMFCs was proposed in the early 1990s [2]. Compared with conventional low-temperature proton exchange membrane fuel cells (LT-PEMFCs) working at around 60°C, HT-PEMFCs with elevated operating temperature feature simpler water and thermal management, higher carbon monoxide (CO) tolerance, faster electrochemical kinetics and easy waste heat recovery via combined heating and power (CHP) systems [3]. Thus, HT-PEMFCs can be applied to the public transportation sector, commercial vehicles, drones and

lightweight aviation, and other stationery and portable power [4]. It has been under development for a wide range of applications by several companies, such as Palcan (300W-30kW, combination methanol-reformer with HT-PEMFCs for power supply) and Advent (1kW-5kW, enable off-grid, portable, auxiliary, CHP or stationary power applications; 15kW-30kW, fitting the needs of trucks, buses, utility, taxis) [4-6].

The proton conduction of the PA-doped PBI membrane does not need the assistance of water, which is one of the major advantages of HT-PEMFCs. In other words, the transport of protons through the membrane does not require water molecules to migrate from the anode to the cathode in the form of hydronium ions (called Vehicle Mechanism), but through structural diffusion, migration occurs between hydrogen bonds (called Grotthuss Mechanism) [7]. Therefore, most of the research on HT-PEMFCs is performed with non-humidified gas. However, water vapor will diffuse from cathode to anode or from anode to cathode in the form of vapor due to the concentration difference and pressure difference between anode and cathode [8]. Moreover, because it works at about 160～180℃, it has good carbon monoxide resistance, so it can be directly fed with the hydrogen-rich reforming gas, which contains a lot of water vapor [9]. Therefore, working in a dead-end mode with pure hydrogen for reducing fuel consumption requires periodical purges because of the dilution of hydrogen on the anode side, caused by the permeation of water vapor from the cathode [10]. The use of anode dead-end mode helps reduce hydrogen consumption and reduces the complexity of the system compared to flow-though mode and hydrogen circulation mode [8]. Besides, at higher operating temperatures, humidifying the reaction gas may helps prevent the dehydration of phosphoric acid into pyrophosphoric acid with lower conductivity, thus prolonging the duriability [11].

Compared with LT-PEMFCs, the research on water vapor transport in HT-PEMFCs is limited. Galbiati et al. [12] verified the phenomenon of water vapor diffusion from the cathode to the anode through experiments and the water vapor transport depends on reactant gas flow rate and humidification. J. Kazdal et al. [13] studied the vapor-liquid equilibrium and evaporation kinetics of water vapor-phosphoric acid and established a

calculation model for the local concentration of PA. In their research, the diffusion coefficient of water vapor in PA is of the order of 10^{-10} m^2/s. In addition, Zhang et al. [14] investigated the performance in anode dead-end mode and flow-through mode and found that due to the accumulation of water vapor, the performance was significantly affected in dead-end mode, and found that up to 31.7% of water vapor is transported from the cathode to the anode. Zhang et al. [15] immediately further did research on water management under this mode-the impact of pressure, drain interval and drain time on performance. Furthermore, Reimer et al. [16] found that the mole fraction of water vapor at the outlet of the anode and cathode is related to the working current density and stoichiometry based on experiments with anode flow-through mode. According to their research, the current and stoichiometry have a certain effect on the diffusion coefficient (2×10^{-7}~3.5×10^{-7} m^2/s) and permeability (5.7×10^{-13}~9.7×10^{-13} mol/(s·cm·Pa)) of water vapor in the PBI membrane. In addition, the water vapor diffusion coefficient in the membrane of 4.47×10^{-5} m^2/s is also reported [10]. Numerical simulation is a useful and powerful tool for understanding more details about the complex phenomena occurring inside the components of the HT-PEMFC, which are very difficult to obtain through experimental studies [17, 18]. Bezmalinovic et al. [10] established a 2-D steady-state HT-PEMFC isothermal model along the direction of the gas channel to investigate the water vapor distribution. Recently, Xia et al. [19] established a 3-D isothermal steady-state model and a 2-D isothermal transient model which is also along the direction of the gas channel. The steady-state model is used to explore the water vapor distribution in HT-PEMFC with different membrane types at different temperatures, and the transient model is used to explore the changes of the water vapor concentration in anode with time when the anode outlet is blcoked.

Although the above numerical models have made a certain contribution to the study of the water vapor distribution, some gaps need to be revealed in HT-PEMFC, such as the influence of the diffusion coefficient of water vapor in the membrane (a big difference in different experiments), the thickness of PBI membrane and catalyst layer (neglected

by previous numerical model), operating conditions as well as the anode operating mode on the distribution of water vapor. Moreover, gas crossover phenomenon of hydrogen and oxygen also affected the water vapor behavior, thus having an impact on water management of HT-PEMFC, which was ignored in previous work.Therefore, in the present work, a novel 3-D iso-nonthermal numerical HT-PEMFC model coupled with the gas-crossover sub-model is developed and validated for investigating above gaps through four aspects. The new contributions and innovations of this research are as following: the sensitivity of the water vapor diffusion coefficient in the PBI membrane under two working temperatures, the influences of the thickness of the membrane and the catalyst layer on the water vapor transport, the influences of operating conditions, relative humidity of hydrogen and pressure difference between anode and cathode are deeply analyzed. In addition, the purge process in the anode dead-end mode is newly explored in HT-PEMFC based on the 3-D non-isothermal transient model.

2. Model description

2.1 Model description and assumptions

Fig. 1(*a*) shows the working principle of HT-PEMFC, namely, reactants (hydrogen, air) are transported by convection and diffusion from the gas channel (GC) to the gas diffusion layer (GDL) and the microporous layer (MPL), then to the catalyst layer (CL) where the electrochemical reactions take place. Hydrogen dissociates into protons and electrons in the anode catalyst layer (ACL). The former is conducted through the membrane (MEM) to the cathode catalyst layer (CCL), the latter is forced to travel in an external circuit (supplying power) to the CCL because the membrane is electrically insulating. In the CCL, oxygen molecules react with the electrons and protons to form water vapor. Meanwhile, part of water vapor diffuses out from the CCL to the GC where it is taken away. Fig. 1 (b) shows the agglomerate structure of CL, revealing the transport of oxygen and water vapor in the CCL. Finally, Fig. 1 (c) shows the computational domain and mesh configuration of the HT-PEMFC model in this

manuscript.

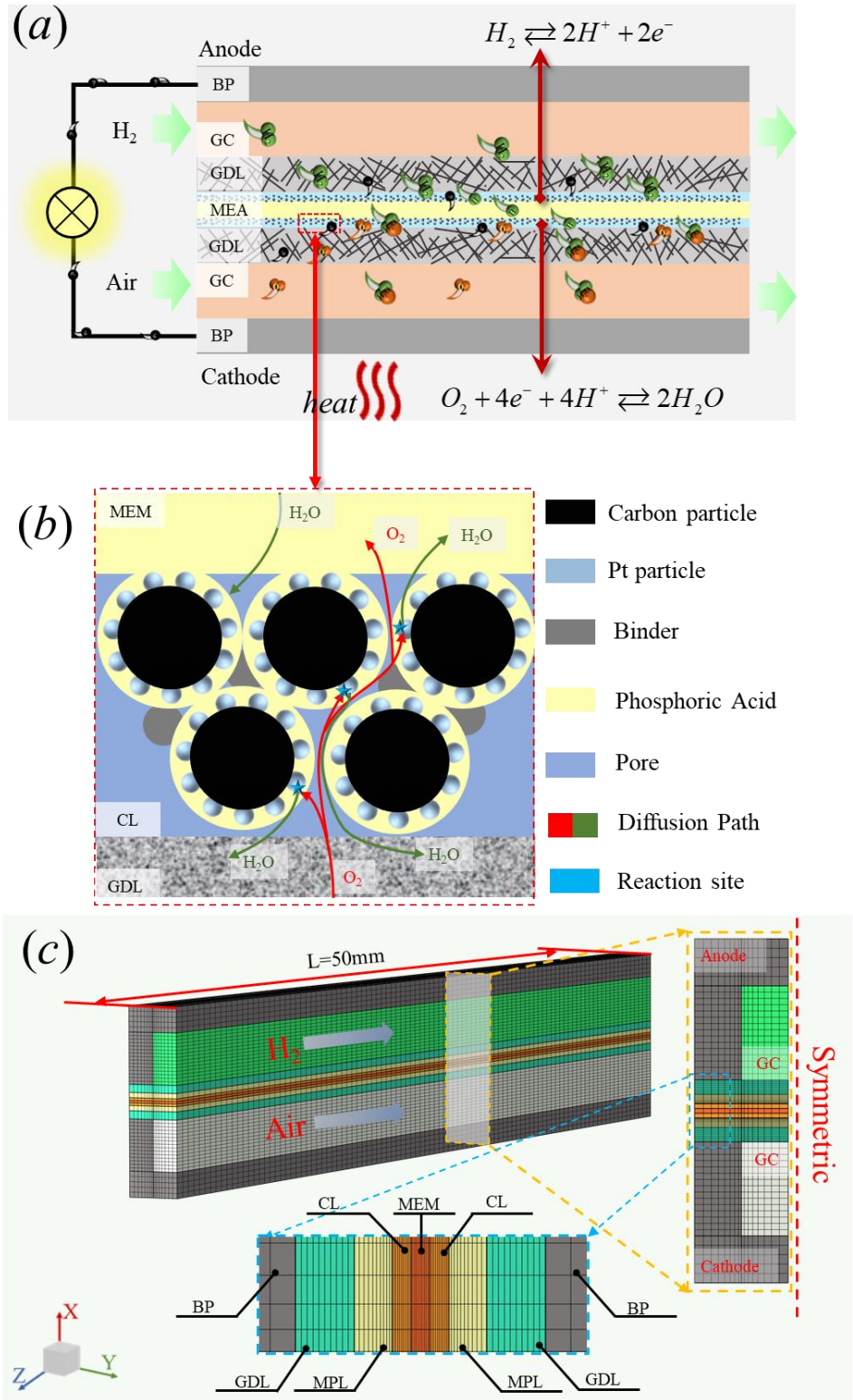

Fig. 1. (*a*) Working principle diagram of HT-PEMFC, (*b*) Illustration of the transport of oxygen and water vapor in the cathode catalyst layer, (*c*) Computational domain and mesh configuration.

Before the numerical model is developed to describe the physical phenomena inside the HT-PEMFC, there are several assumptions as follows[18, 20]: 1) gases are ideal due to low presure; 2) gas flow is laminar due to low velocit; 3) porous media material is isotropic and homogeneous; 4) Radiative heat transfer is not considered; 5) The viscous effect of fluid flow results in fluid heating is neglected because of the lower velocity.

2.2 Gas-crossover model

Ideally, the PA-doped PBI membrane only allows protons to pass through. However, since the membrane is a porous material, and the reaction gas is dissolved in phosphoric acid, expressed by Henry's Law (Eq. (1)), thus hydrogen can permeate from anode to cathode through the membrane (called hydrogen crossover), while oxygen can permeate from cathode to anode (called oxygen crossover). Moreover, as mentioned before, due to the concentration gradient and pressure gradient, water vapor also diffuses from the cathode to the anode or from the anode to the cathode [15]. Because of facile hydrogen oxidation kinetic and higher overpotential at the CCL, the hydrogen crossover through the membrane can be oxidized electrochemically at the CCL, while the oxygen crossover through the membrane leads to catalytic combustion at the ACL because of lower overpotential within ACL [21, 22].

$$\begin{aligned} C_{O_2}^{H} &= x_{O_2} \cdot p_c \cdot H_{O_2} \\ C_{H_2}^{H} &= x_{H_2} \cdot p_a \cdot H_{H_2} \end{aligned} \tag{1}$$

This paper assumes that the crossover hydrogen is completely oxidized in the CCL, and the crossover oxygen is completely react with hydrogen in the ACL. The effects of crossover hydrogen, oxygen and water vapor on the mass, energy, species, current can be found in Table 1. ΔH represents the amount of heat produced by the complete chemical reaction of per mole of hydrogen with oxygen, which equals $241{,}845\ J/mol$ [23].

Table 1. The source/sink term caused by gas crossover [10, 23]

Description	Correlation	Unit
Current	$J_{H_2}^{cross} = 2F \cdot n_{H_2}^{cross} = 2F \cdot D_{H_2}^{PA} \cdot \frac{C_{H_2}^{H}}{t_{MEM}}$ (CCL)	A/m^3
Species and mass	$S_{O_2}^{cross} = \frac{-J_{H_2}^{cross}}{4Ft_{CL}}$ $S_{H_2O,c}^{cross} = \frac{J_{H_2}^{cross}}{2Ft_{CL}} - D_{H_2O}^{MEM} \frac{C_{H_2O}^{CCL} - C_{H_2O}^{ACL}}{t_{MEM}} M_{H_2O}$ (CCL) $S_{H_2}^{cross} = \frac{-2n_{O_2}^{cross}}{t_{CL}}$ $S_{H_2O,a}^{cross} = \frac{2n_{O_2}^{cross}}{t_{CL}} = \frac{2D_{O_2}^{PA} \times C_{O_2}^{H}}{t_{CL} \times t_{MEM}} + D_{H_2O}^{MEM} \frac{C_{H_2O}^{CCL} - C_{H_2O}^{ACL}}{t_{MEM}} M_{H_2O}$ (ACL)	$kg/(m^3 \cdot s)$
Energy	$S_{T,c}^{cross} = \frac{-J_{H_2}^{cross}}{t_{CL}} \left(\eta_C + T \frac{dE_{eq}^{c}}{dT} \right)$ (CCL) $S_{T,a}^{cross} = -\Delta H \cdot S_{H_2}^{cross}$ (ACL)	W/m^3

2.3 Governing equations and Additional constitutive equations

As shown in Fig. 1 (b), the governing equations contain current, mass, momentum, species and energy conservation equations. The governing equations of this model are described as follows.

Mass conservation equation (computational domain: GC, GDL, MPL, CL),

$$\nabla \cdot \left(\varepsilon \rho_g \vec{u} \right) = S_m \tag{2}$$

Where the ε is porosity and it's equal to 1 in the gas channel, ρ_g is the gas density which can be calculated by ideal gas law,

$$\rho_g = p \left(RT \sum_i^N \frac{\omega_i}{M_i} \right)^{-1} \tag{3}$$

Momentum conservation equation (computational domain: GC, GDL, MPL, CL),

$$\frac{\rho_g}{\varepsilon^2} \left(\vec{u} \cdot \nabla \right) \vec{u} = \nabla \cdot \left[-p\vec{I} + \vec{K} \right] - \frac{S_m}{\varepsilon^2} \vec{u} + S_u \tag{4}$$

Where the $\vec{K}(Pa)$ is the viscous stress tensor. For the Newtonian fluid, it can be calculated by the following expression,

$$\vec{K} = \frac{\mu}{\varepsilon}\left(\nabla\vec{u} + \left(\nabla\vec{u}\right)^T\right) - \frac{2}{3}\frac{\mu}{\varepsilon}\left(\nabla\cdot\vec{u}\right)\vec{I} \tag{5}$$

Where the $\mu\left(kg/\left(m\cdot s\right)\right)$ is the dynamic viscosity of mixture gas which can be calculated based on the kinetic theory,

$$\mu = \sum_{i=1}^{N}\frac{x_i\mu_i}{\sum_{j=1}^{N}x_j\phi_{ij}} \tag{6}$$

$$\phi_{ij} = \frac{\left[1+\left(\mu_i/\mu_j\right)^{1/2}\left(M_j/M_i\right)^{1/4}\right]^2}{\left[8\left(1+M_j/M_i\right)\right]^{1/2}} \tag{7}$$

Energy conservation equation (All domain),

$$\left(\rho \mathrm{C}_p\right)^{eff}\vec{u}\cdot\nabla T - \nabla\cdot k^{eff}\nabla T = S_T \tag{8}$$

Where the effective volumetric heat capacity, $\left(\rho \mathrm{C}_p\right)^{eff}$, and the effective thermal conductivity, $k^{eff}\left(W/\left(m\cdot K\right)\right)$, of GDL, MPL and CL is defined as,

$$\left(\rho C_p\right)^{eff} = \sum_i\left(\theta_i\rho_i C_{p,i}\right) + \left(1\text{-}\sum_i\theta_i\right)\rho_g C_{p,g} \tag{9}$$

$$k^{eff} = \sum_i\left(\theta_i k_i\right) + \left(1\text{-}\sum_i\theta_i\right)k_g \tag{10}$$

For the thermal conductivity of mixture gas is also calculated by the kinetic theory, just replace the dynamic viscosity in Eq. (6) and (7) into the thermal conductivity of gas components. And the heat capacity mixture gas can be calculated by,

$$C_{p,g} = \sum_{i=1}^{N}\omega_i\left(C_p\right)_i \tag{11}$$

Species conservation equation (computational domain: GC, GDL, MPL, CL),

$$\rho_g\left(\vec{u}\cdot\nabla\right)\omega_i=\nabla\cdot\left(\rho\omega_i\sum_{j=1}^{N}D_{i-j}^{eff}\overrightarrow{d_j}\right)+S_i \tag{12}$$

The Maxwell-Stefan model is applied to define the diffusional driving force $\overrightarrow{d_j}$,

$$\overrightarrow{d_j}=\nabla x_j+\frac{1}{p}\left(\nabla x_j-\omega_j\right)\nabla p \tag{13}$$

Where the x_j represents mole fraction of $j\text{-}th$ species and it can be calculated by,

$$x_j=\frac{\omega_j}{M_j}\left(\sum_i^n\frac{\omega_i}{M_i}\right)^{-1} \tag{14}$$

Moreover, the effective binary diffusion coefficient, D_{i-j}^{eff}, in the porous regions (CL, GDL, MPL) is modified by the Bruggeman correlation,

$$D_{i\text{-}j}^{eff}=\varepsilon^{1.5}D_{i-j} \tag{15}$$

Current conservation equation (computational domain: BP, GDL, MPL, CL, MEM),

$$\begin{aligned}&Electron:\nabla\left(\kappa_{ele}^{eff}\nabla\varphi_{ele}\right)=S_\varphi\\&Proton:\ \nabla\left(\kappa_{ion}^{eff}\nabla\varphi_{ion}\right)=-S_\varphi\end{aligned} \tag{16}$$

Where the effective electron conductivity, κ_{ele}^{eff}, and the effective proton conductivity, κ_{ion}^{eff}, of CL are also corrected by Bruggeman correlation based on the porosity and electrolyte volume fraction of CL,

$$\kappa_{ele}^{eff}=\left(1-\varepsilon-\nu\right)^{1.5}\kappa_{ele} \tag{17}$$

$$\kappa_{ion}^{eff}=\nu^{1.5}\kappa_{ion} \tag{18}$$

Where the proton conductivity is correlated with temperature, the doping level (DL) of PA in the PBI membrane as well as the surrounding relative humidity (RH) [24]:

$$\kappa_{ion}=\delta^{eff}\frac{ab}{T}\exp\left(\frac{-E_{MEM}}{RT}\right) \tag{19}$$

Where a and b are the two different pre-exponential factors and $E_{MEM}\,(J/mol)$ is the activation energy, and $\delta^{eff}=1.35$ is the correction factor.

$$\begin{aligned} a &= 168DL^3 - 6,324DL^2 + 65,760DL + 8,460 \\ E_{MEM} &= -619.6DL + 21750 \\ b &= \begin{cases} 1+(0.01704T-4.767)RH^{eff} & 373.15K \le T \le 413.15K \\ 1+(0.1432T-56.89)RH^{eff} & 413.15K \le T \le 453.15K \\ 1+(0.7T-309.2)RH^{eff} & 453.15K \le T \le 473.15K \end{cases} \end{aligned} \tag{20}$$

The relevant source/sink terms mentioned above are listed in Table 2. Where $J_a, J_c\left(A/m^3\right)$ represents the volume exchange current density,

$$J = \begin{cases} j_{H_2}^{ref} \cdot ECSA_a^{eff} \cdot \left(\dfrac{C_{H_2}}{C_{H_2}^{ref}}\right)^{0.5} \cdot \left(\exp\left(\dfrac{\alpha_a F \eta_a}{RT}\right) - \exp\left(\dfrac{-\alpha_c F \eta_a}{RT}\right)\right) & Anode \\ j_{O_2}^{ref} \cdot ECSA_c^{eff} \cdot \left(\dfrac{C_{O_2}}{C_{O_2}^{ref}}\right) \cdot \left(\exp\left(\dfrac{\alpha_a F \eta_c}{RT}\right) - \exp\left(\dfrac{-\alpha_c F \eta_c}{RT}\right)\right) & Cathode \end{cases} \tag{21}$$

Where $\eta(V)$ represents the overpotential in anode and cathode CL, which can be calculated by,

$$\eta = \varphi_{ele} - \varphi_{ion} - E_{eq} \tag{22}$$

Where E_{eq} is the equilibrium potential (also called reversible thermodynamic voltage), which can be calculated by the Nernst equation,

$$E_{eq} = \begin{cases} 0 & \text{Anode} \\ 1.185 - 2.3\times10^{-4}\left(T-298.15\right) + \dfrac{RT}{2F}\left(\ln p_{H_2}^{in} + \dfrac{1}{2}\ln p_{O_2}^{in}\right) & \text{Cathode} \end{cases} \tag{23}$$

The equilibrium potential should be corrected by subtracting the open circuit voltage loss due to H_2 and O_2 crossover and short-circuiting [25]. According to Ref. [26], the open-circuit voltage is 0.96V, so it is determined that the loss is 0.3729V $(@T=160℃)$.

The electrochemical reaction parameters used in the model are summarized in Table 3. Additionally, the cell dimensions, material properties and operating conditions are listed in Table 4.

Table 2. Source/sink terms of HT-PEMFC model

Source/Sink terms	Unit
$S_m = S_{H_2} + S_{O_2} + S_{H_2O}$	$kg/(m^3 \cdot s)$
$S_{H_2} = \begin{cases} -\dfrac{J_a M_{H_2}}{2F} + S_{H_2}^{cross} & (ACL) \\ 0 & (other\ zone) \end{cases}$ $\quad S_{O_2} = \begin{cases} 0 & (other\ zone) \\ -\dfrac{J_c M_{O_2}}{4F} + S_{O_2}^{cross} & (CCL) \end{cases}$	
$S_{H_2O} = \begin{cases} S_{H_2O,a}^{cross} & (ACL) \\ \dfrac{J_c M_{H_2O}}{4F} + S_{H_2O,c}^{cross} & (CCL) \\ 0 & (other\ zone) \end{cases}$	$kg/(m^3 \cdot s)$
$S_\varphi = \begin{cases} J_a & (ACL) \\ J_c + J_{H_2}^{cross} & (CCL) \\ 0 & \text{(other zone)} \end{cases}$	A/m^3
$S_u = \begin{cases} -k\vec{u}/\mu & (CL\ ,\ GDL,\ MPL) \\ 0 & (other\ zone) \end{cases}$	$kg/(m^2 \cdot s^2)$
$S_T = \begin{cases} J_a \lvert\eta_a\rvert + \lVert\nabla\varphi_{ele}\rVert^2 \kappa_{ele}^{eff} + \lVert\nabla\varphi_{ion}\rVert^2 \kappa_{ion}^{eff} + S_{T,a}^{cross} & \text{(ACL)} \\ J_c \left(\lvert\eta_c\rvert + \left\lvert T \dfrac{dE_{eq}^c}{dT} \right\rvert \right) + \lVert\nabla\varphi_{ele}\rVert^2 \kappa_{ele}^{eff} + \lVert\nabla\varphi_{ion}\rVert^2 \kappa_{ion}^{eff} + S_{T,c}^{cross} & \text{(CCL)} \\ \lVert\nabla\varphi_{ele}\rVert^2 \kappa_{ele}^{eff} & \text{(GDL ,MPL, BP)} \\ \lVert\nabla\varphi_{ion}\rVert^2 \kappa_{ion}^{eff} & \text{(MEM)} \end{cases}$	W/m^3

Table 3. HT-PEMFC model: Electrochemical Properties [3, 27-31]

Description	Correlation/Value (T in K)
Exchange current density	$j_{H_2}^{ref} = j_a^{ref} \exp[-1400(\frac{1}{T} - \frac{1}{353.15})]$ $j_{O_2}^{ref} = j_c^{ref} \exp[-7900(\frac{1}{T} - \frac{1}{353.15})]$
Reference exchange current density	$j_a^{ref} = 1\times10^4\ A/m^2$ $j_c^{ref} = 0.04\ A/m^2$
Electrochemical surface area	$ECSA_a^{eff} = ECSA_c^{eff} = 1\times10^5\ 1/m$
Transfer coefficients	$\alpha_a = 1, \alpha_c = 1$
Reference molar concentration	$C_{H_2}^{ref} = 40.88\,\mathrm{mol}/m^3$ $C_{O_2}^{ref} = 40.88\,\mathrm{mol}/m^3$

Table 4. Cell properties, Operation condition and Species properties [10, 18]

Description	Value
GC length/width/depth; rib width	50/1/1mm; 1mm
Thickness of GDL; MPL	0.255mm; 0.1mm
Thickness of CL; MEM	0.05mm; 0.05mm
Electrical conductivity of CL; GDL; MPL; BP	$\kappa_{ele} = 450; 1250; 1000; 14000\ S/m$
The density of CL; GDL; MPL; BP; MEM	$\rho = 2145; 450; 2719; 2266; 1300\ kg/m^3$
Specific heat capacity of CL; GDL; MPL; BP; MEM	$C_p = 3300; 568; 871; 1580; 1650\ J/(kg \cdot K)$
Thermal conductivity of CL; GDL; MPL; BP; MEM	$k = 1.5; 1.5; 1; 1.2; 20\ W/m{\cdot}K$
Permeability of CL; GDL; MPL	$K = 6.2\mathrm{e}^{-13};\ 6.2\mathrm{e}^{-12}\ ; 6.2\mathrm{e}^{-13} m^2$
Porosity of CL; GDL;MPL	$\varepsilon = 0.3; 0.7; 0.3$

The volume fraction of electrolyte in CL	$\nu = 0.2$
Doping Level of PA molecules per PBI repeat unit	$DL = 11$
Stoichiometric ratio	$\zeta_a = 1.5,\ \zeta_c = 2.5$
Reference current density	$j^{ref} = 1.5 A/cm^2$
Operation temperature	$T_{opt} = 180°C/160°C$
Reference humidity of inlet gas	$RH_a = RH_c = 0$

Species Transport Parameters	Correlation/Value (T in K, p in Pa)	Unit
Dynamic viscosity	$\mu_{H_2} = 3.205\times10^{-3}(T/293.85)^{1.5}(T+72)^{-1}$ $\mu_{O_2} = 8.46\times10^{-3}(T/292.25)^{1.5}(T+127)^{-1}$ $\mu_{H_2O} = 7.512\times10^{-3}(T/291.15)^{1.5}(T+120)^{-1}$ $\mu_{N_2} = 7.33\times10^{-3}(T/300.15)^{1.5}(T+111)^{-1}$	$kg/(m\cdot s)$
Binary diffusion coefficient	$D_{i-j} = D_{i-j}^{ref}(T/403.15)^{1.5}(101325/p)$ $D_{H_2-H_2O}^{ref} = 1.405\times10^{-4}$ $D_{O_2-H_2O}^{ref} = 4.53\times10^{-5}$ $D_{O_2-N_2}^{ref} = 3.45\times10^{-5}$ $D_{N_2-H_2O}^{ref} = 4.48\times10^{-5}$	m^2/s
Diffusion coefficient of water vapor in the membrane	$D_{H_2O}^{MEM} = 4.77\times10^{-5}$	m^2/s
Specific heat capacity of species	$(C_p)_{H_2} = 14283$ $(C_p)_{H_2O(g)} = 2014$ $(C_p)_{N_2} = 1040.67$ $(C_p)_{O_2} = 919.31$	$J/(kg\cdot K)$
Thermal conductivity of species	$k_{H_2} = 0.1672$ $k_{H_2O(g)} = 0.0261$ $k_{N_2} = 0.0242$ $k_{O_2} = 0.0246$	$W/(m\cdot K)$

2.4 Boundary conditions and Numerical implementation

To accurately obtain the numerical solution, the boundary conditions of each physical field are carefully considered as follows:

1) Secondary current distribution: The outer surface of the anode bipolar plate is

set with zero voltage and the outer surface of the cathode bipolar plate is set with operating voltage.

2) Free and porous media flow: The fully developed flow is used at the inlet of the gas channel, and the inlet velocity is determined by reference current density, the stoichiometric ratio, as well as the inlet molar concentration. The outlet of the gas channel is set at 1*atm* (absolute pressure),

$$U_{a,in} = \frac{\zeta_a j^{ref} A_{CL}}{2FA_{a,in} C_{H_2,in}},\ U_{c,in} = \frac{\zeta_c j^{ref} A_{CL}}{4FA_{c,in} C_{O_2,in}} \tag{24}$$

3) Transport of concentrated species: The inlet molar concentration of hydrogen and oxygen which are determined by the humidity, temperature, and pressure of the inlet, where the inlet pressure is equal to the outlet pressure add the pressure drop,

$$C_{H_2,in} = \frac{P_{out}^a + \Delta P^a - RH_a \cdot P_{sat}}{RT_{opt}}, C_{O_2,in} = \frac{0.21\left(P_{out}^c + \Delta P^c - RH_c \cdot P_{sat}\right)}{RT_{opt}} \tag{25}$$

where $P_{sat}\left(atm\right)$ is the vapor saturation pressure which depends on temperature $\Delta T = T - 273.15$,

$$\log_{10} P_{sat} = -2.1794 + 0.02953 \times \Delta T - 9.1837e^{-5} \times \Delta T^2 + 1.4454e^{-7} \times \Delta T^3 \tag{26}$$

4) Heat transfer: Thermal boundary condition specified on the outer surface of BP is $T_{BP} = T_{opt}$. Heat flux is specified at the gas channel inlet,

$$q = \rho_g \vec{u}\left[\int_{T_{in}}^{T} C_p dT + \int_{p_{in}}^{p} \frac{1}{\rho}\left(1 - \chi T\right) dp\right] \tag{27}$$

where χ (1/K) represents the coefficient of thermal expansion, for the ideal gas, $\chi = 1/T$. Additionally, symmetrical boundary conditions and no-slip boundary conditions are applied on the side surfaces normal to Y-axis [18].

After setting the boundary conditions, the numerical model is discretized and solved

using the finite element method (FEM), and the separate solution method is adopted, so that different solve method can be used to solve different conservation equations, which reduces computational power requirements and increases convergence. The computational domain is divided into 80,000 hexahedral elements, as shown in Fig. 1 (c), and grid independence research has been carried out in previous research [3, 32], and the relative error is set $1e^{-5}$.

3. Results and discussion

3.1 Model validation

The simulated polarization curves are compared with experimental data obtained from Ref. [26] under different temperatures. Fig. 2 displays the comparison and the consistency is acceptable [33]. The maximum error between experiment and simulation is less than 0.05A/cm^2. It should be noted that parameters of cell properties and operating conditions are the same as those in Table 4, and it is set as the same as the experiment in Ref. [26].

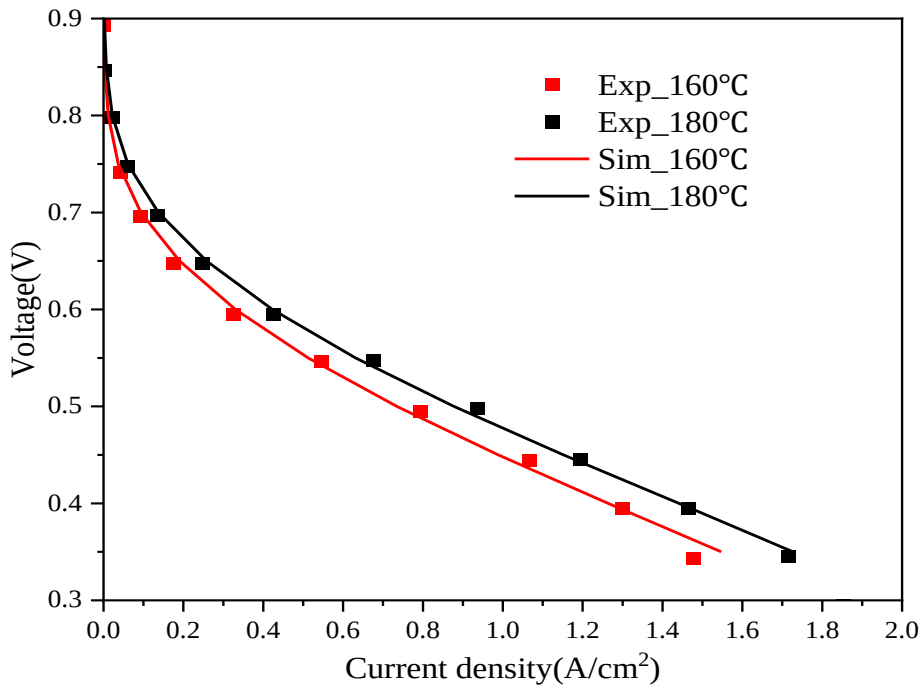

Fig. 2 Comparison of polarization curves between simulation results of this research and experimental data under different temperatures.

3.2 Sensitivity analysis of water vapor transport coefficient

Due to the different types of high-temperature proton exchange membrane and the difference in the assembly process of the stack, the diffusion coefficients of water vapor in the membrane reported in the literature are quite different, even with several orders of magnitude differences. Therefore, the sensitivity analysis of the water vapor transport coefficient in the membrane under different working temperatures and voltages without humidification reaction gas is conducted in this section, expressed by Eq. (28), where β is sensitivity coefficient.

$$D_{H_2O_eff}^{MEM} = \beta \times D_{H_2O}^{MEM} \tag{28}$$

Fig. 3 shows the effect of temperature and voltage on water vapor transport flux from cathode to anode under different water vapor transport coefficients. It can be seen that as the voltage decreases, the operating temperature increases, the flux of water vapor transfer at per unit time increases [16]. This can be explained by the following reasons. According to the output characteristics of the fuel cell, as the terminal voltage drops, the current rises, thus more water vapor is produced at the cathode catalyst layer per unit time, so more water vapor diffuses to the anode. In addition, the increase in temperature also speeds up the electrochemical reaction rate and improves the performance of the fuel cell, so more water vapor is produced at the CCL. It can also be seen that when the sensitivity is less than 1, the water vapor transport flux increases sharply with the increase of the sensitivity coefficient, and when the sensitivity coefficient is greater than 1, it is almost unchanged. In the anode flow-through mode, water vapor is not easy to accumulate in the gas channel or porous medium, so the performance of the fuel cell is almost unchanged under different water vapor diffusion coefficients [15].

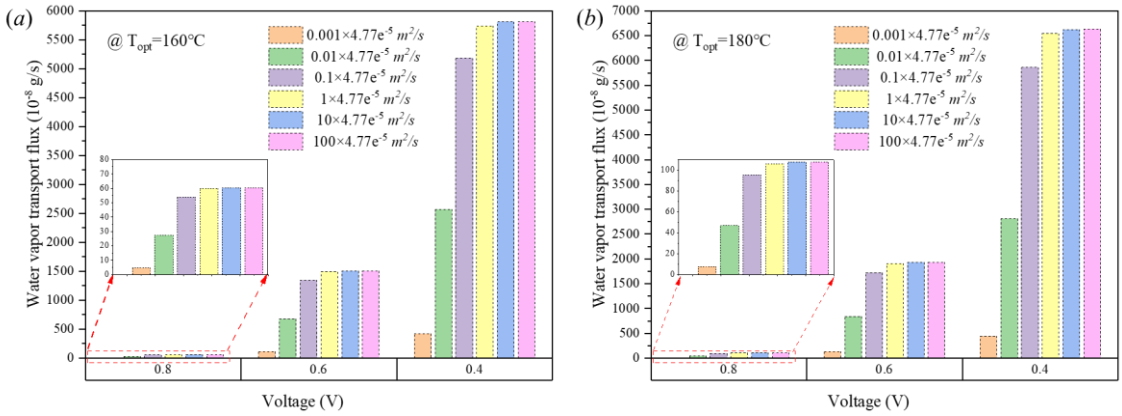

Fig. 3 Water vapor transport flux from cathode to anode under different water vapor transport coefficients at three different working voltages. *a*) $T_{opt} = 160℃$, *b*) $T_{opt} = 180℃$

Fig. 4 displays the influence of different water vapor transport coefficients on the distribution of water vapor molar concentration in the middle plane of the ACL and the CCL at the temperature of 160℃ and the voltage of 0.4V. The water vapor transport coefficient has almost no effect on the water distribution of the ACL, but has a significant effect on the water distribution of the CCL, especially when the sensitivity coefficient is less than 1. This is because as the diffusion coefficient of water vapor increases, more water vapor generated in the CCL can diffuse to the anode, which is consistent with the analysis result in Fig. 3. When the sensitivity coefficient is greater than 1, water vapor on both sides of the PBI membrane can reach dynamic equilibrium, so the water vapor molar concentration of the CCL does not change too much. Since both hydrogen and air are dry gases, and water vapor is generated in the CCL, the water vapor concentration of the CCL is higher than that of the ACL.

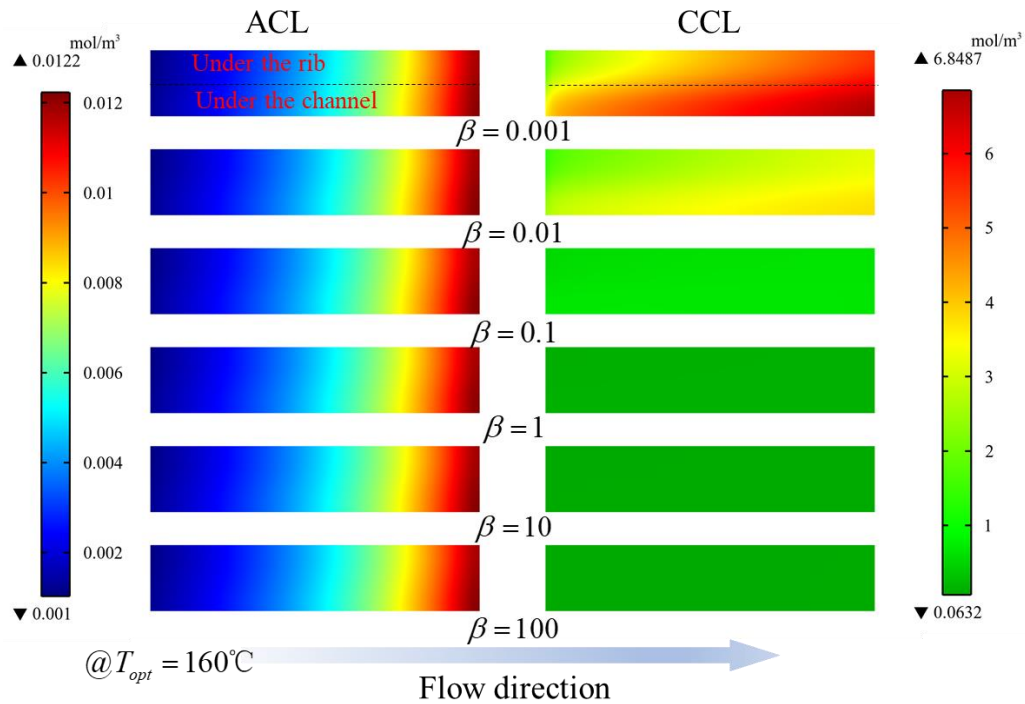

Fig. 4 Influence of different water transport coefficients on the distribution of water vapor molar concentration in the middle plane of the ACL and the CCL.

According to the sensitivity analysis, when the sensitivity coefficient is greater than 1, the concentration and transport flux does not change much. Therefore, in the subsequent simulation analysis, the sensitivity coefficients are all set to 1.

3.3 Thickness influence of membrane and catalyst layer on water vapor transport

As the thickness of the membrane increases, the diffusion distance of protons increases, which lowers the cell performance. The electrochemical active reaction area increases with the increasing thickness of the catalyst layer, making cell performance improvement [20] Fig. 5 (a) and (b) shows the effect of PBI membrane thickness and catalyst layer thickness on the water vapor transportation flux from cathode to anode. It can be found that the influence of thickness on flux is consistent with the trend of performance changes (see Supplementary Information Fig. S1). However, at 0.8V, although the membrane thickness has almost no effect on performance, the water vapor transport flux decreases with the increase of the membrane thickness due to the longer

diffusion path length.

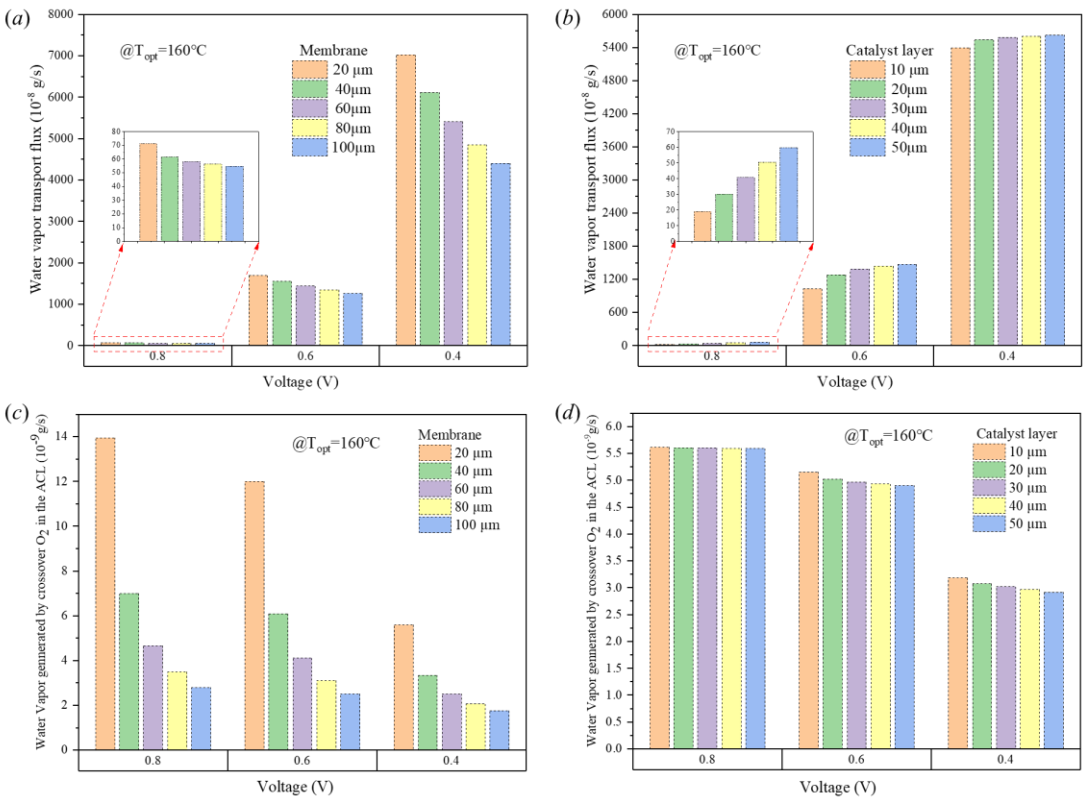

Fig. 5 Effect of PBI membrane thickness and catalyst layer thickness on the water vapor transport flux and on the amount of water vapor generates in the ACL caused by the crossover oxygen. (a) and (c) PBI membrane, (b) and (d) Catalyst layer.

The effect of membrane thickness and catalyst layer thickness on the amount of water vapor generated in the ACL caused by crossover oxygen is shown in Fig. 5 (c) and (d)**Error! Reference source not found.**. Compared with the water vapor flux transported from the cathode to the anode, the water vapor content generated in the ACL is 4~5 orders of magnitude lower. In addition, it can be seen from**Error! Reference source not found.**that the higher the voltage, the higher the water vapor content generated in the ACL. This is because when the voltage is high, the cathode oxygen concentration is high so that more oxygen diffuses to the anode, thus more water vapor is produced in the ACL due to the direct reaction between H_2 and O_2. As the membrane thickness increases, the water vapor output at the ACL also gradually decreases, which is due to the increase in the diffusion path length of oxygen in the

membrane. However, as the thickness of the catalyst layer increases, the amount of water vapor generated in the ACL is unchanged at 0.8V, and the amount of water vapor generated gradually decreases at 0.6V and 0.4V. This is because increasing the thickness improves the HT-PEMFC performance so that more oxygen is consumed in the CCL, thereby reducing the oxygen concentration.

3.4 Relative humidity influence of hydrogen on water transport

Fig. 6 shows the effect of relative humidity (RH) (at $T_{RH} = 60℃$) of hydrogen in the inlet on the water vapor transport flux. With the increasing relative humidity of the hydrogen, more water vapor diffuses back from the anode to the cathode. When the relative humidity of hydrogen is 0, water vapor diffuses from the cathode to the anode at any voltage, and the flux of water vapor increases with decreasing voltage. When the relative humidity of hydrogen is in the range of 20% to 40%, water vapor diffuses back from the anode to the cathode at a voltage of 0.6V to 0.8V. However, at 0.4V, water vapor still diffuses from the cathode to the anode. When the relative humidity of hydrogen is higher than 60%, water vapor always diffuses from the anode to the cathode. This analysis result shows that proper humidification of hydrogen will help prevent the phosphoric acid in the catalyst layer from losing water when working at medium and high voltages to become pyrophosphoric acid with poor proton conductivity [9]. And to avoid over-humidification of hydrogen causing water vapor diffuses from the anode to the cathode, reducing oxygen concentration and thus reducing performance, the humidity of hydrogen should be less than 60%(@T=60℃).

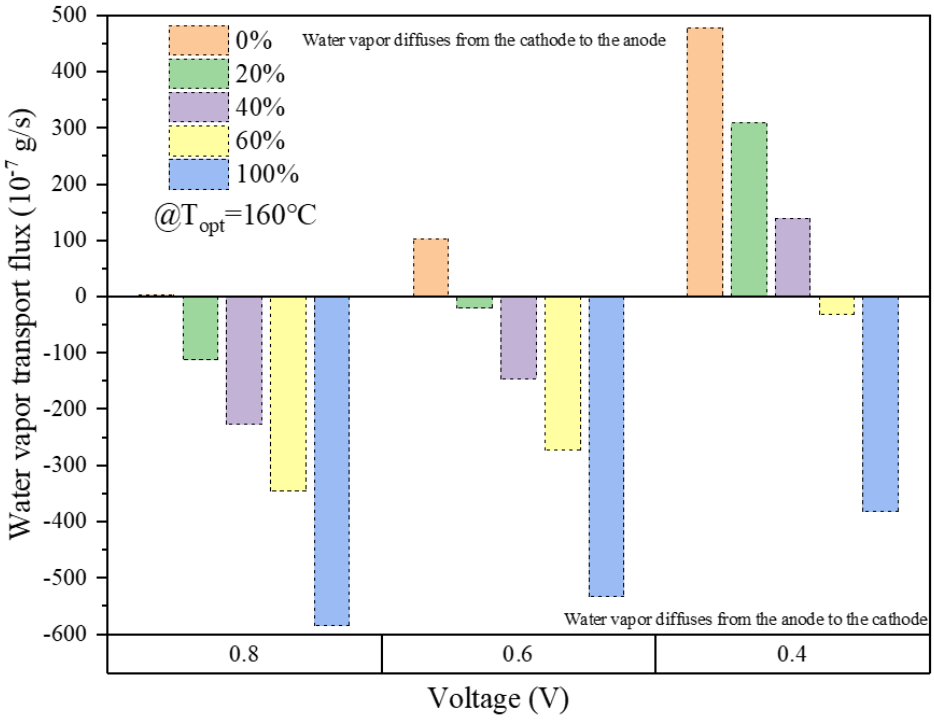

Fig. 6 Effect of relativity humidity of anode on the water vapor transport flux.

The distribution of water vapor concentration and flux at the interface between CL and MEM are shown in Fig. 7. Under different voltages, the water vapor concentration distribution trend does not change. At the anode, the distribution of water vapor under the gas channel and the rib are almost the same, but the water vapor under the gas channel on the cathode side is much smaller than the water vapor concentration under the rib. This is mainly because the inlet velocity of the cathode is almost four times that of the anode. As the voltage increases, the water vapor concentration both for anode and cathode decreases.

From Fig. 7 (c), in the case of 0.6V and 0.8V, water vapor diffuses from the anode to the cathode no matter it is under the rib or the gas channel. In addition, the diffusion flux under the gas channel is higher than the flux under the rib and the closer to the inlet, the higher the diffusion flux. It is worth noting that the smaller the negative value in the legend, the greater the diffusion flux from the anode to the cathode. At 0.4V, water vapor diffuses back from the anode to the cathode, mainly in the area below the gas channel, and also diffuses from the cathode to the anode, mainly in the area under the rib. The white line in this figure is the contour line where the water vapor diffusion

flux is zero [10]. The reason why the diffusion flux of water vapor from the anode to the cathode under the rib is lower or even the diffusion from the cathode to the anode occurs is because of the higher water vapor concentration under the rib on the cathode.

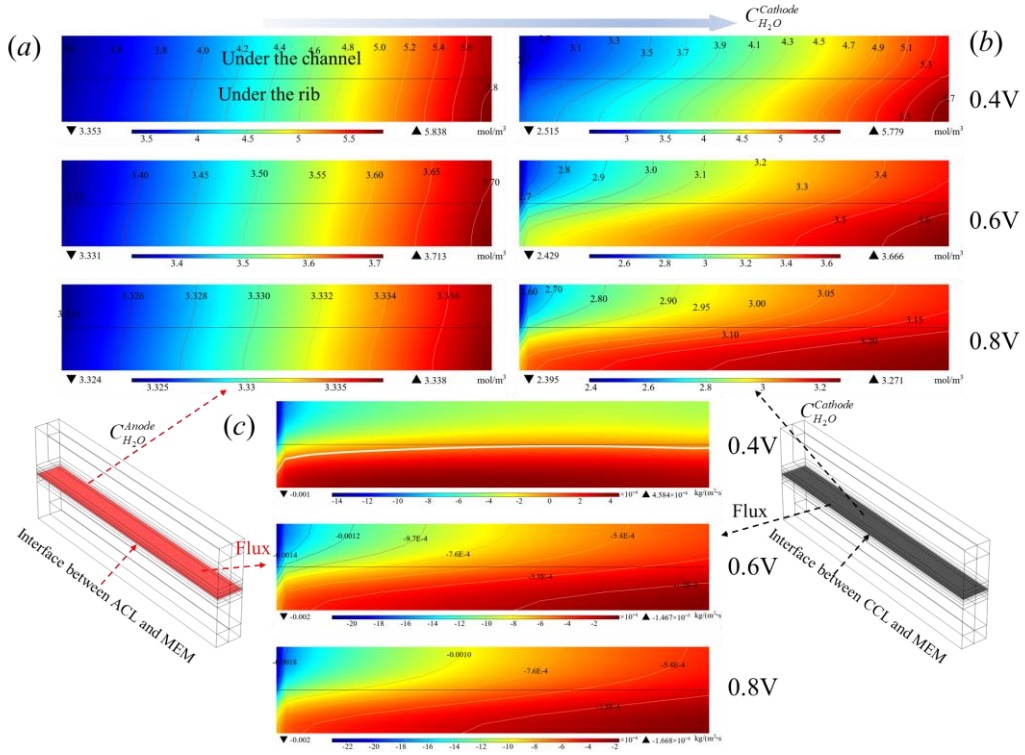

Fig. 7 Distribution of water vapor concentration and transport flux distribution at the interface between the catalyst layer and the membrane with RH of 60%. (a) Water vapor concentration distribution of anode, (b) Water vapor concentration distribution of cathode, (c) Distribution of water vapor transport flux between cathode and anode.

3.5 Pressure difference influence between anode and cathode on water transport

In this section, the effect of the pressure difference between anode and cathode on the water vapor transport is investigated. In the analysis, the outlet pressure of one side is maintained at atmospheric pressure (absolute pressure) and the outlet pressure of the other side is increased.

Fig. 8 shows the transport flux of water vapor under different pressure differences and different voltages. When the cathode pressure remains constant, as the anode pressure

increases, the water vapor flux from the anode to the cathode increases. When the anode pressure remains constant, it is the opposite as the cathode pressure increases. This is because the concentration of water vapor increases with increasing pressure [15], as shown in Fig. 9, thereby enhancing or inhibiting the transport of water vapor between the cathode and the anode. Moreover, when the voltage is 0.4V, water vapor even diffuses from the cathode to the anode as the cathode pressure increases. To make the water vapor generated in the CCL diffuse back to the anode and avoid the loss of water in the phosphoric acid at the anode, it is necessary to make the cathode pressure 0.2 bar higher than that of the anode.

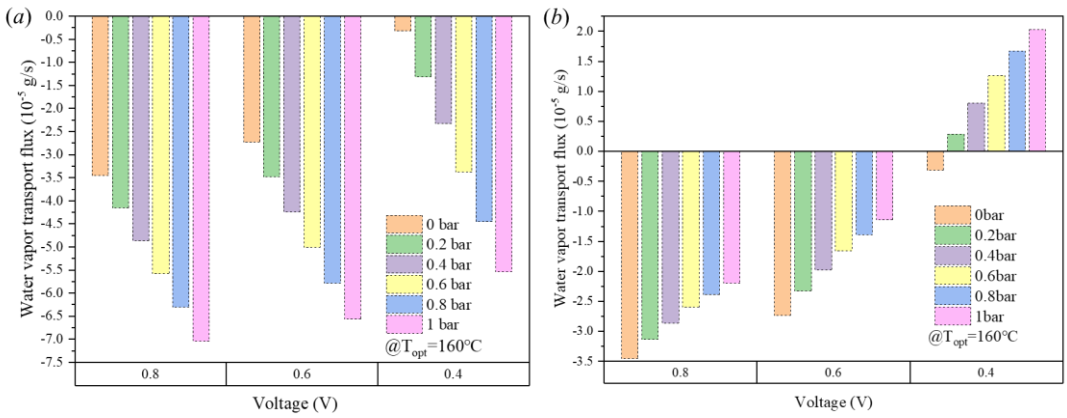

Fig. 8 Effect of the pressure difference between anode and cathode on the water vapor transport flux with RH of hydrogen is 60% at 60 ℃. (a) Higher anode pressure, (b) Higher cathode pressure

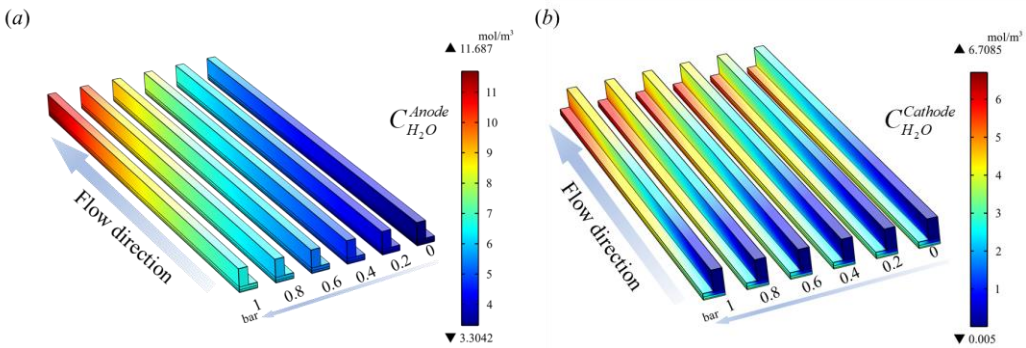

Fig. 9 Effect of the pressure difference between anode and cathode on the water vapor concentration at 0.4V with RH of hydrogen is 60% at 60 ℃. (a) Anode, (b) Cathode.

Because pressure changes also affect the crossover-diffusion of hydrogen and oxygen and therefore affect the water vapor generated by the crossover-diffusion of H_2 and O_2. As can be seen from

Fig. 10 (a) and (d), the change of anode pressure has almost no effect on the water vapor content due to oxygen crossover-diffusion produced in the ACL. The variation of cathode pressure and output voltage has little effect on the water vapor content due to hydrogen crossover-diffusion produced in the CCL. This is because the hydrogen crossover is mainly depended on the concentration and partial pressure of H_2 in the ACL which has little variation. However, as can be seen from

Fig. 10 (b) and (c), the amount of water vapor generated by hydrogen crossover-diffusion in the CCL increases with increasing anode pressure, and the amount of water vapor generated by oxygen crossover-diffusion in the ACL increases with increasing cathode pressure.

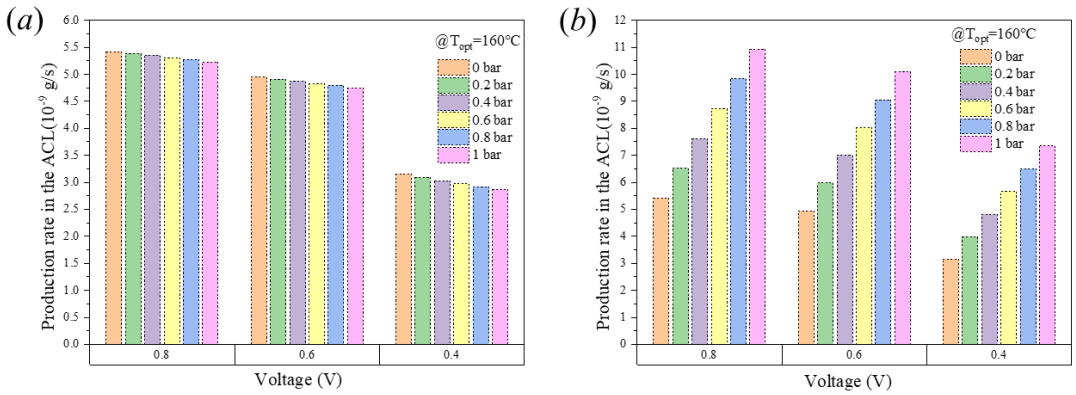

Water vapor generated by the crossover O_2

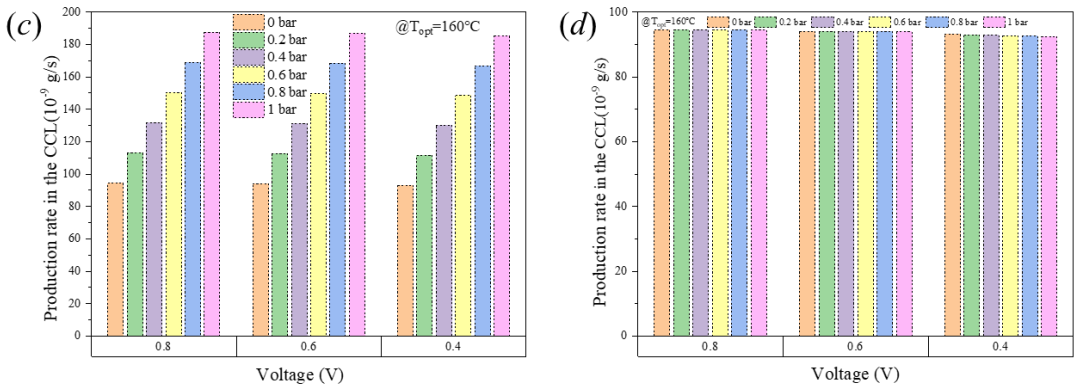

Water vapor generated by the crossover H_2

Fig. 10 Effect of the pressure difference between anode and cathode on the water vapor generated caused by crossover H_2 and O_2 in ACL and CCL. (a) and (c) Anode pressure is higher than cathode pressure, (b) and (d) Anode pressure is lower than cathode pressure.

3.6 Vapor behavior during the purge process at the anode with dead-end mode

Although HT-PEMFC does not produce liquid water during normal operation, previous studies have confirmed the diffusion of a large amount of water vapor from the cathode to the anode, resulting in performance degradation in dead-end mode [14]. Therefore, in this section, A 3-D transient non-isothermal HT-PEMFC numerical model is developed in the present work to investigate the purge process. This is slightly different from the previous steady-state model. A time term is added to the left side of each conservation equation. Second, the anode inlet uses a pressure inlet (20Pa, relative pressure), and the anode outlet uses a periodic pressure (see Supplementary Information Fig. S2) to simulate the open and close of the anode outlet. It should be noted that the time term of water vapor transport in the membrane is not considered in the present work. In other words, the water vapor concentration of anode and cathode is in dynamic equilibrium. Moreover, the maximum time step of the solution process is set to 0.02s [19]. To reduce the requirements for computing resources and shorten the computing time, this simulation is carried out under a larger current.

It can be seen from Fig. S2 that when the anode outlet is blocked, the output performance drops sharply, and when the anode outlet is opened, the performance recovers [14]. This is mainly due to the diffusion of water vapor from the cathode to the anode, which causes the accumulation of water vapor at the anode outlet, reducing the concentration of hydrogen, as shown in Fig. 11. Moreover, it can be found that the current density drops rapidly between 21.2s and 22.4s, similar to the results in Ref. [15], which is due to the water vapor concentration at the anode end increasing rapidly. In addition, after a purge, performance recovers quickly and accumulated water vapor is

quickly discharged.

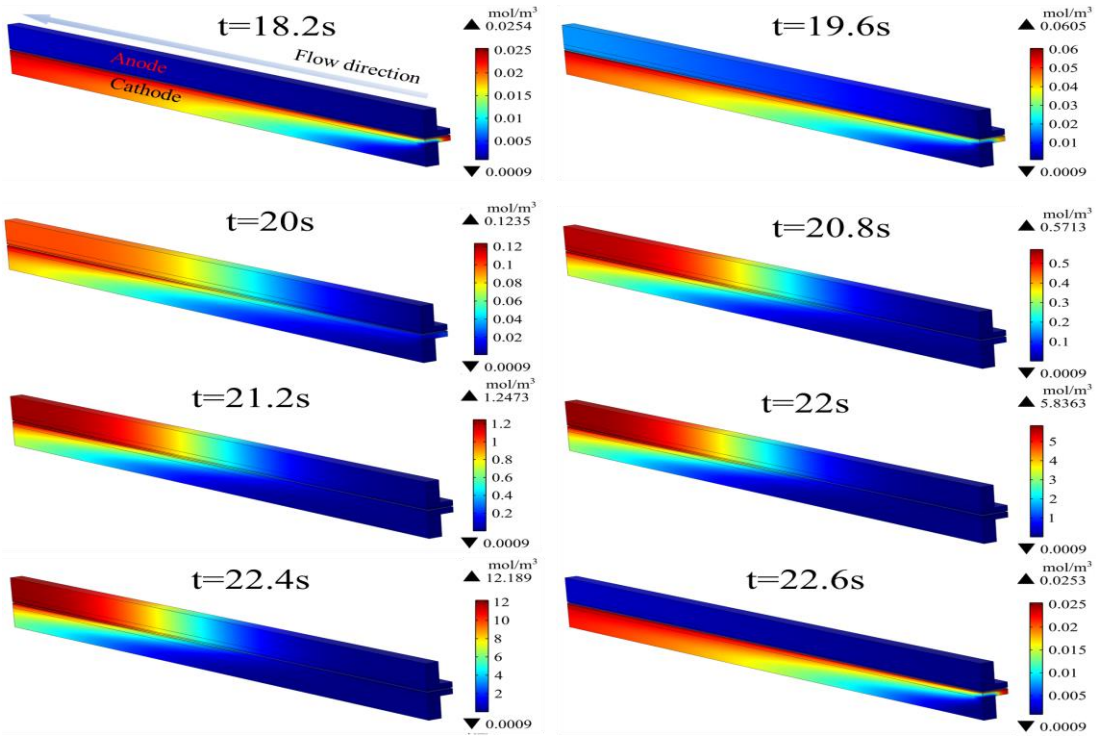

Fig. 11 The variation of water vapor concentration distribution in a purge cycle (18.2s-22.6s).

4. Conclusions

In the present work, a novel 3-D non-isothermal high-temperature proton exchange membrane fuel cell (HT-PEMFC) numerical model is developed coupling gas-crossover phenomena forinvestigating the water vapor behavior, which is useful for improving the water management and performance of HT-PEMFC. The key works and results of this research as below.

First, the sensitivity of the water diffusion coefficients was carried out and found that the transportation flux of water does not change when the order of magnitude of the water vapor diffusion coefficient is higher than 10^{-5}. Then, the influence of the thickness of the membrane and the catalyst layer is also explored. As the thickness of the membrane increases, the water transport flux decreases, but as the catalyst layer thickness increases, the water transport flux increases slightly. After that, It is found that increasing the humidity of hydrogen promotes the diffusion of water vapor from

the anode to the cathode, and inhibits the diffusion of water vapor from the cathode to the anode. And increasing anode pressure or decreasing cathode pressure has the same effect. Thus, it suggested that the humidity of hydrogen should be less than 60% (@T=60□) and the cathode side pressure should be higher than the anode side pressure by more than 0.2bar to aovid water vapor in anode diffusion to cathode. In addition, as the voltage drops or the operating temperature rises, it can facilitate the diffusion of water vapor from the cathode to the anode. Finally, the purge process is also simulated by the dynamical numerical model. When the anode outlet is blocked, water vapor continues to accumulate at the anode outlet, which reduces the concentration of hydrogen, thereby causing a reversible decline in performance. After purging, the performance is restored.

Acknowledge

This work is supported in part by the National Natural Science Foundation of China (51806024), the Technological Innovation and Application Demonstration in Chongqing (Major Themes of Industry: cstc2019jscx-fxyd0158, cstc2019jscx-zdztzxX0033). M. Ni thanks the grants (PolyU 152064/18E) from Research Grant Council, University Grants Committee, Hong Kong SAR.

Reference

[1] Deng M, Zhang Q, Huang Y, Zhang X. Integration and optimization for a PEMFC and PSA oxygen production combined system. Energy Convers Manage. 2021;236.
[2] Li Q, Aili D, Hjuler HA, Jensen, Oluf JOJ. High temperature polymer electrolyte membrane fuel cells. J Springer Switzerland. 2016:387-425.
[3] Zhang J, Zhang C, Hao D, Ni M, Huang S, Liu D, et al. 3D non-isothermal dynamic simulation of high temperature proton exchange membrane fuel cell in the start-up process. Int J Hydrogen Energy. 2021;46:2577-93.
[4] Advent Technologies Holdings I. https://www.advent.energy/advent-power-stacks. 2021.
[5] Dipl.-Phy AB, Head of Fuel Cell Systems Group, Oel-Waerme-Institut, Herzogenrath, Germany. OWI for methanol reformer/HT-PEMFC system, truck APU. Fuel Cells Bulletin. 2013;2013:10.
[6] http://www.palcan.com.cn/application_1.html. 2021.
[7] Li Q, Jensen JO, Savinell RF, Bjerrum NJ. High temperature proton exchange membranes based on polybenzimidazoles for fuel cells. Prog Polym Sci. 2009;34:449-

77.
[8] Chen B, Zhou H, He S, Meng K, Liu Y, Cai Y. Numerical simulation on purge strategy of proton exchange membrane fuel cell with dead-ended anode. Energy. 2021;234.
[9] Zhou F, Singdeo D, Kær SK. Investigation of the Effect of Humidity Level of H_2 on Cell Performance of a HT□PEM Fuel Cell. Fuel Cells. 2019;19:2-9.
[10] Bezmalinović D, Strahl S, Roda V, Husar A. Water transport study in a high temperature proton exchange membrane fuel cell stack. Int J Hydrogen Energy. 2014;39:10627-40.
[11] Zhou F, Andreasen SJ, Kær SK, Park JO. Experimental investigation of carbon monoxide poisoning effect on a PBI/H3PO4 high temperature polymer electrolyte membrane fuel cell: Influence of anode humidification and carbon dioxide. Int J Hydrogen Energy. 2015;40:14932-41.
[12] Galbiati S, Baricci A, Casalegno A, Marchesi R. Experimental study of water transport in a polybenzimidazole-based high temperature PEMFC. Int J Hydrogen Energy. 2012;37:2462-9.
[13] Kazdal TJ, Lang S, Kühl F, Hampe MJ. Modelling of the vapour–liquid equilibrium of water and the in situ concentration of H3PO4 in a high temperature proton exchange membrane fuel cell. J Power Sources. 2014;249:446-56.
[14] Zhang C, Zhang L, Zhou W, Wang Y, Chan SH. Investigation of water transport and its effect on performance of high-temperature PEM fuel cells. Electrochim Acta. 2014;149:271-7.
[15] Zhang C, Zhou W, Zhang L, Chan SH, Wang Y. An experimental study on anode water management in high temperature PEM fuel cell. Int J Hydrogen Energy. 2015;40:4666-72.
[16] Reimer U, Ehlert J, Janßen H, Lehnert W. Water distribution in high temperature polymer electrolyte fuel cells. Int J Hydrogen Energy. 2016;41:1837-45.
[17] Samris A, Mounir H, El Marjani A. Effect of platinum dispersity, platinum loading and Pt-Oxide coverage on oxygen reduction reaction in PEMFC-Cathode. J Electroanal Chem. 2021;895.
[18] Zhang J, Zhang C, Li J, Deng B, Fan M, Ni M, et al. Multi-perspective analysis of CO poisoning in high-temperature proton exchange membrane fuel cell stack via numerical investigation. Renewable Energy. 2021;180:313-28.
[19] Lingchao X, Caizhi Z, Chen J, Chen L, Ni M, Bo D, et al. Numerical study of vapor behavior in high temperature PEM fuel cell under key material and operating parameters. International Journal of Green Energy. 2021:1-12.
[20] Xia L, Zhang C, Hu M, Jiang S, Chin CS, Gao Z, et al. Investigation of parameter effects on the performance of high-temperature PEM fuel cell. Int J Hydrogen Energy. 2018;43:23441-9.
[21] Chippar P, Ju H. Numerical modeling and investigation of gas crossover effects in high temperature proton exchange membrane (PEM) fuel cells. Int J Hydrogen Energy. 2013;38:7704-14.
[22] Tang Q, Li B, Yang D, Ming P, Zhang C, Wang Y. Review of hydrogen crossover through the polymer electrolyte membrane. Int J Hydrogen Energy. 2021;46:22040-61.

[23] Nam J, Chippar P, Kim W, Ju H. Numerical analysis of gas crossover effects in polymer electrolyte fuel cells (PEFCs). Applied Energy. 2010;87:3699-709.
[24] Jiao K, Li X. A Three-Dimensional Non-isothermal Model of High Temperature Proton Exchange Membrane Fuel Cells with Phosphoric Acid Doped Polybenzimidazole Membranes. Fuel Cells. 2010;10:351-62.
[25] Ren P, Pei P, Li Y, Wu Z, Chen D, Huang S. Degradation mechanisms of proton exchange membrane fuel cell under typical automotive operating conditions. Prog Energy Combust Sci. 2020;80.
[26] Devrim Y, Albostan A, Devrim H. Experimental investigation of CO tolerance in high temperature PEM fuel cells. Int J Hydrogen Energy. 2018;43:18672-81.
[27] Li WK, Zhang QL, Wang C, Yan XH, Shen SY, Xia GF, et al. Experimental and numerical analysis of a three-dimensional flow field for PEMFCs. Appl Energ. 2017;195:278-88.
[28] Oh K, Jeong G, Cho E, Kim W, Ju H. A CO poisoning model for high-temperature proton exchange membrane fuel cells comprising phosphoric acid-doped polybenzimidazole membranes. Int J Hydrogen Energy. 2014;39:21915-26.
[29] Boaventura M, Sousa JM, Mendes A. A dynamic model for high temperature polymer electrolyte membrane fuel cells. Int J Hydrogen Energy. 2011;36:9842-54.
[30] Oh K, Ju H. Temperature dependence of CO poisoning in high-temperature proton exchange membrane fuel cells with phosphoric acid-doped polybenzimidazole membranes. Int J Hydrogen Energy. 2015;40:7743-53.
[31] Zhang Z, Liu W, Wang Y. Three dimensional two-phase and non-isothermal numerical simulation of multi-channels PEMFC. International Journal of Hydrogen Energy. 2019;44:379-88.
[32] Xia L, Ni M, Xu Q, Xu H, Zheng K. Optimization of catalyst layer thickness for achieving high performance and low cost of high temperature proton exchange membrane fuel cell. Applied Energy. 2021;294.
[33] Xing L, Song X, Scott K, Pickert V, Cao W. Multi-variable optimisation of PEMFC cathodes based on surrogate modelling. Int J Hydrogen Energy. 2013;38:14295-313.

Click here to access/download;Figure;figure.pptx

Graphical Abstract

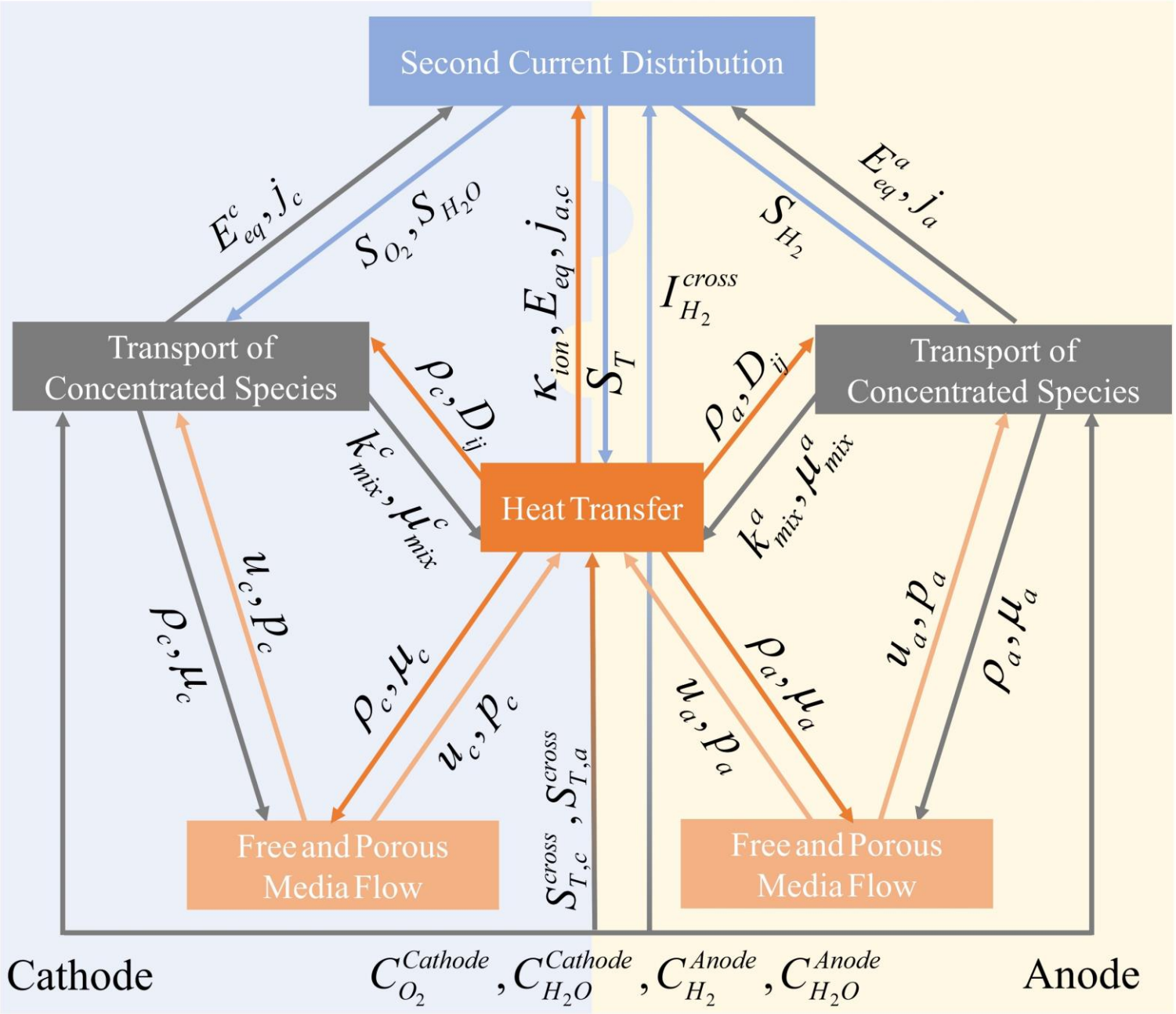

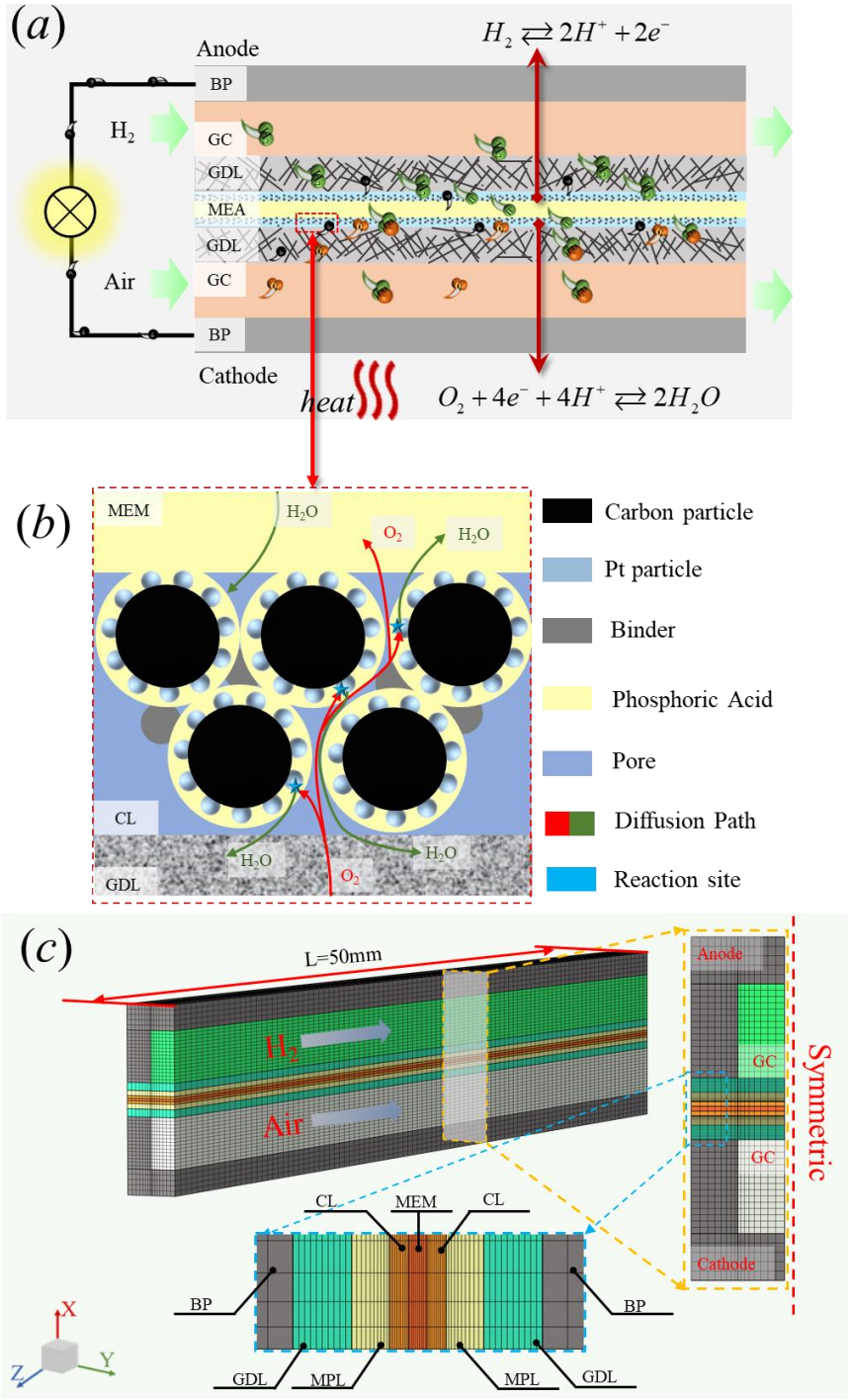

Fig. 1. (*a*) Working principle diagram of HT-PEMFC, (*b*) Illustration of the transport of oxygen and water vapor in the cathode catalyst layer, (*c*) Computational domain and mesh configuration.

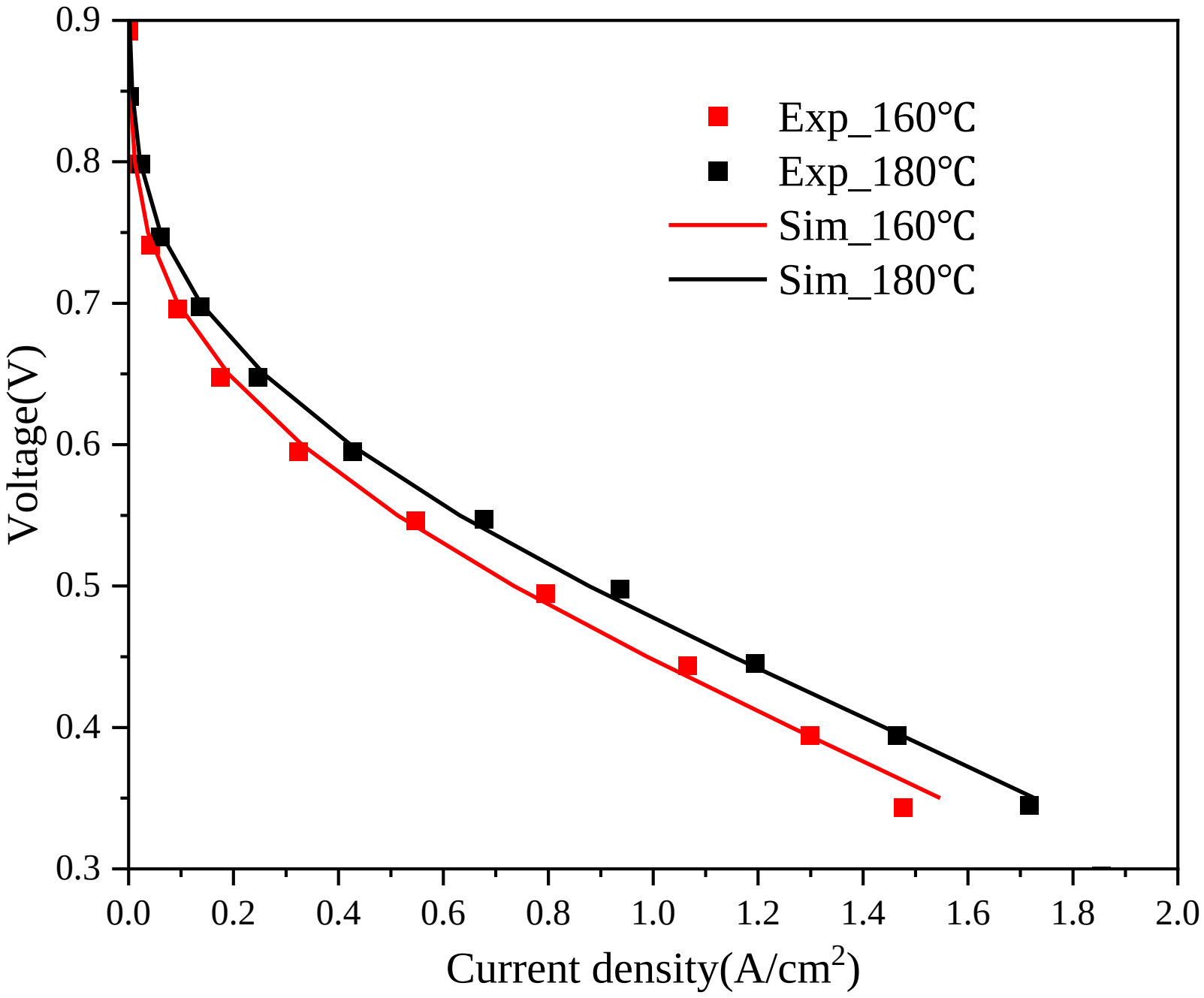

Fig. 2 Comparison of polarization curves between simulation results of this study and experimental data under different temperatures.

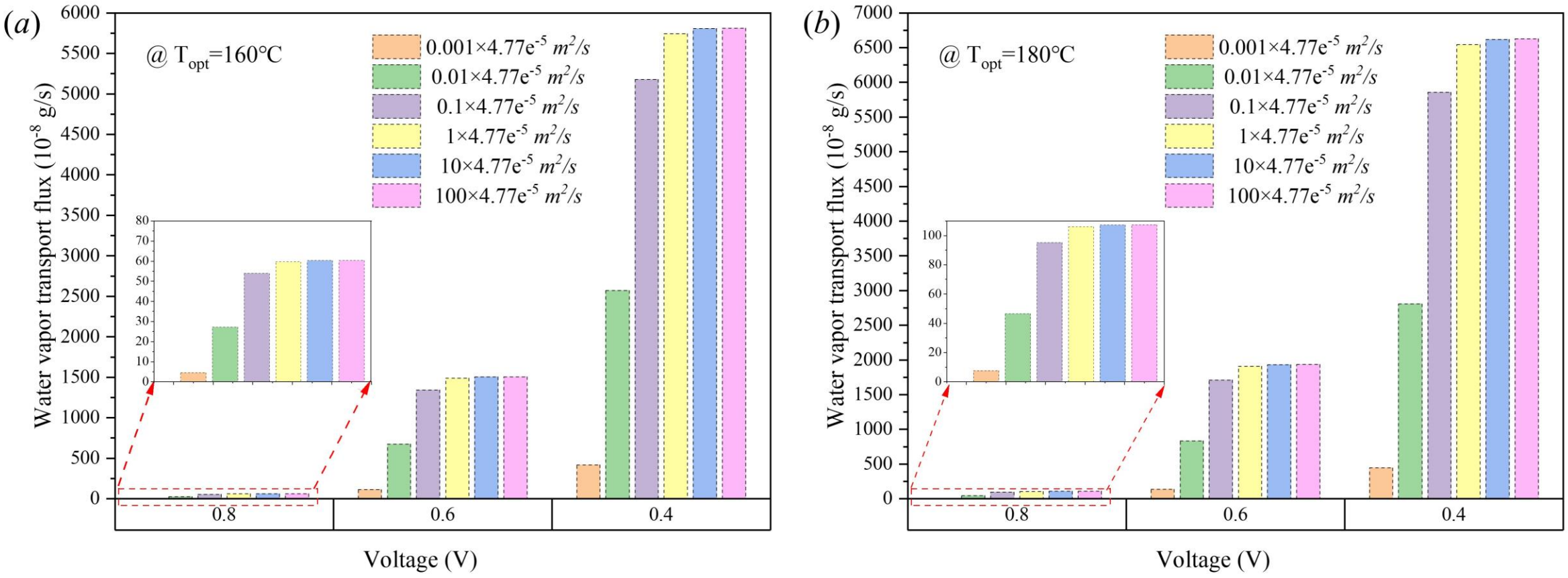

Fig. 3 Water vapor transport flux from cathode to anode under different water vapor transport coefficients at three different working voltages. *a*) $T_{opt} = 160℃$, *b*) $T_{opt} = 180℃$

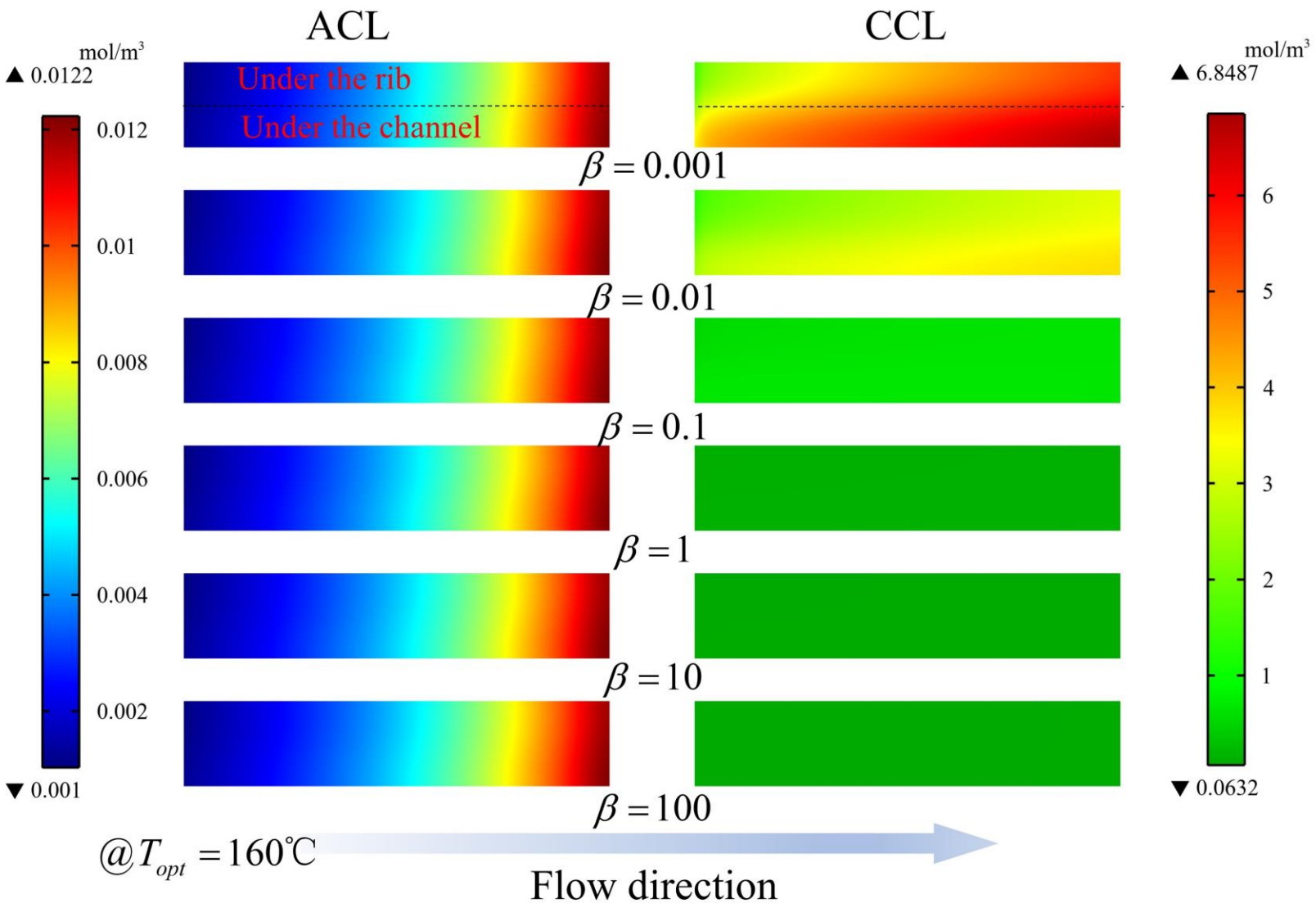

Fig. 4 Influence of different water transport coefficients on the distribution of water vapor molar concentration in the middle plane of the ACL and the CCL.

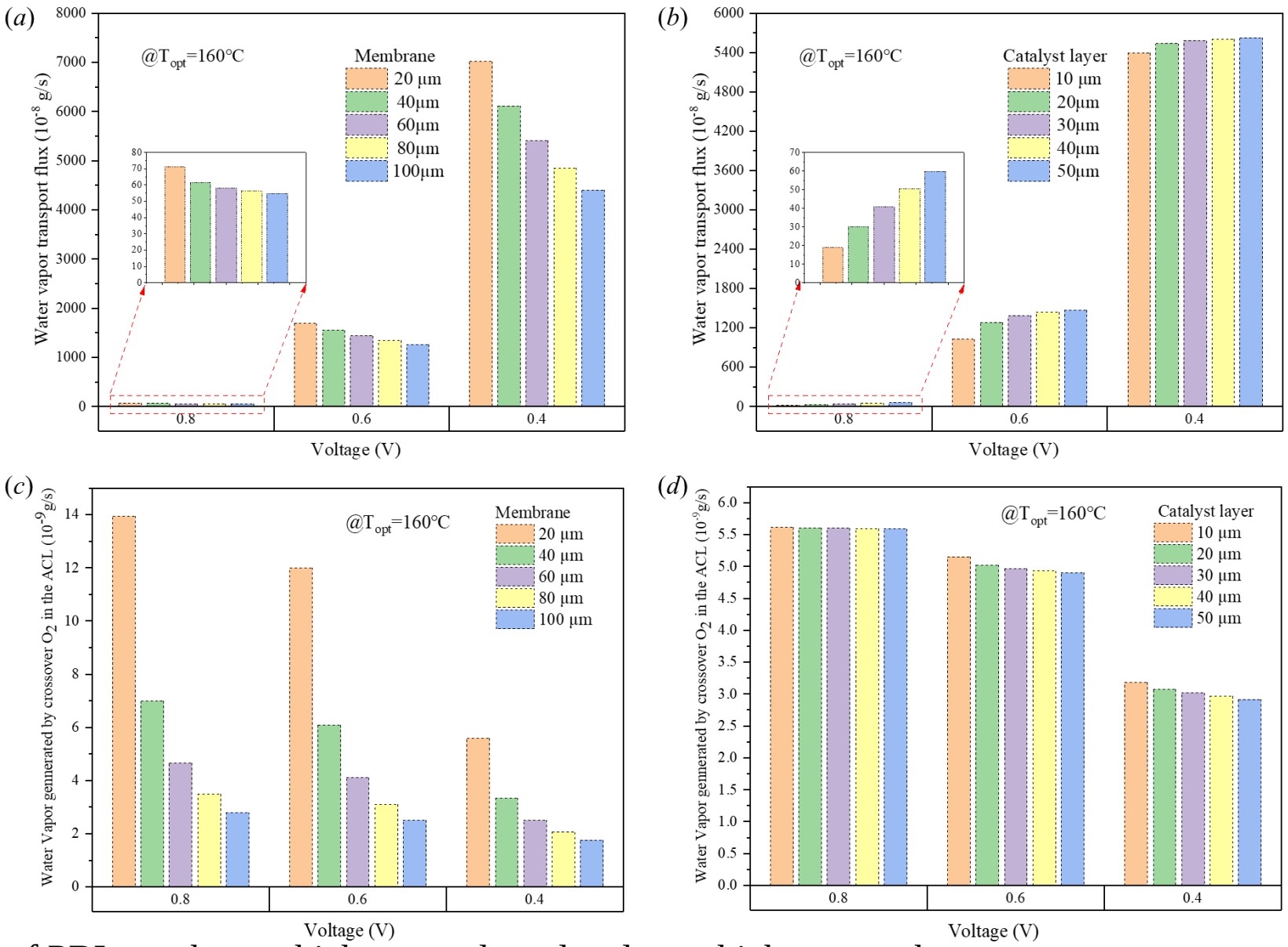

Fig. 5 Effect of PBI membrane thickness and catalyst layer thickness on the water vapor transport flux and on the amount of water vapor generates in the ACL caused by the crossover oxygen. (a) and (c) PBI membrane, (b) and (d) Catalyst layer.

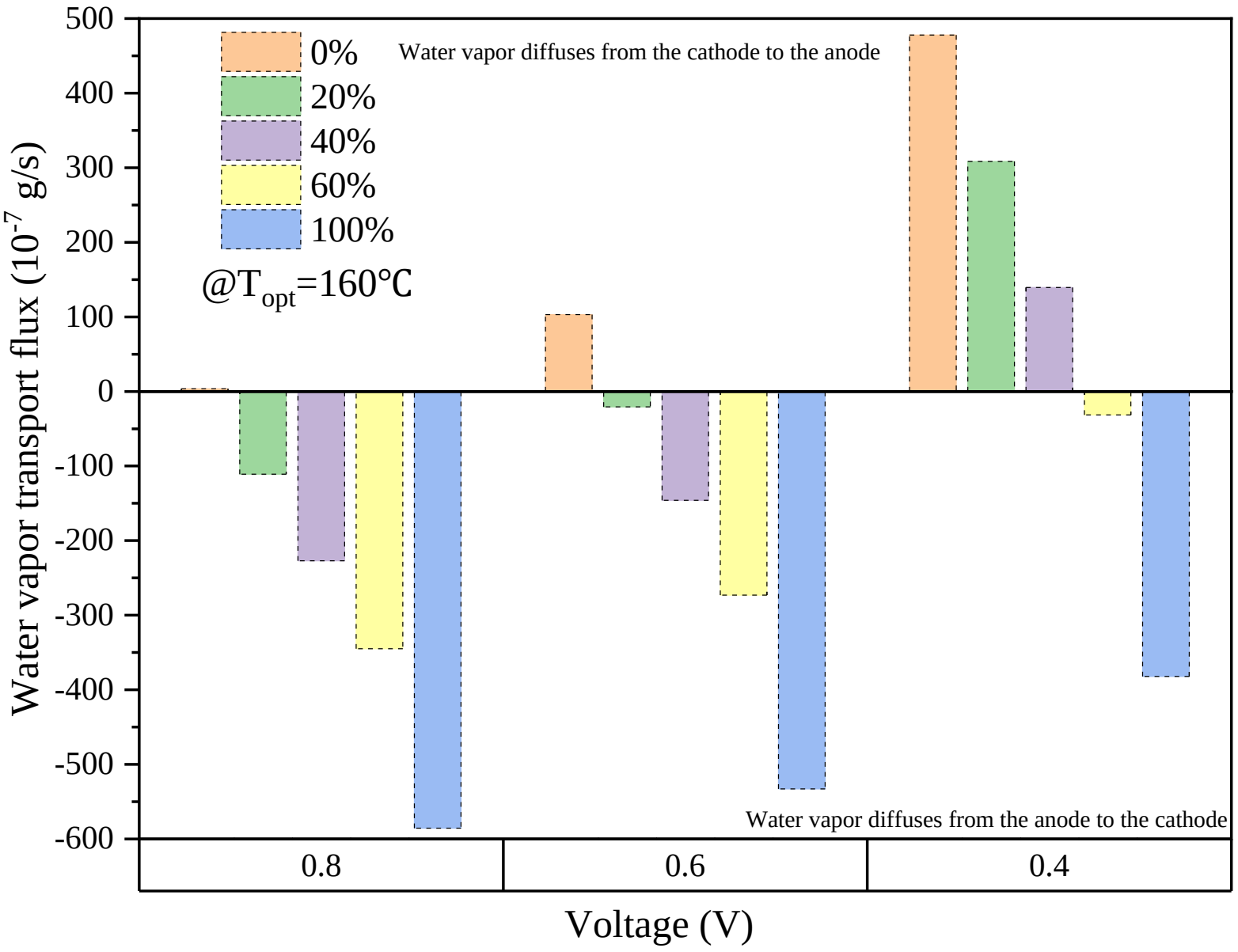

Fig. 6 Effect of relativity humidity of anode on the water vapor transport flux.

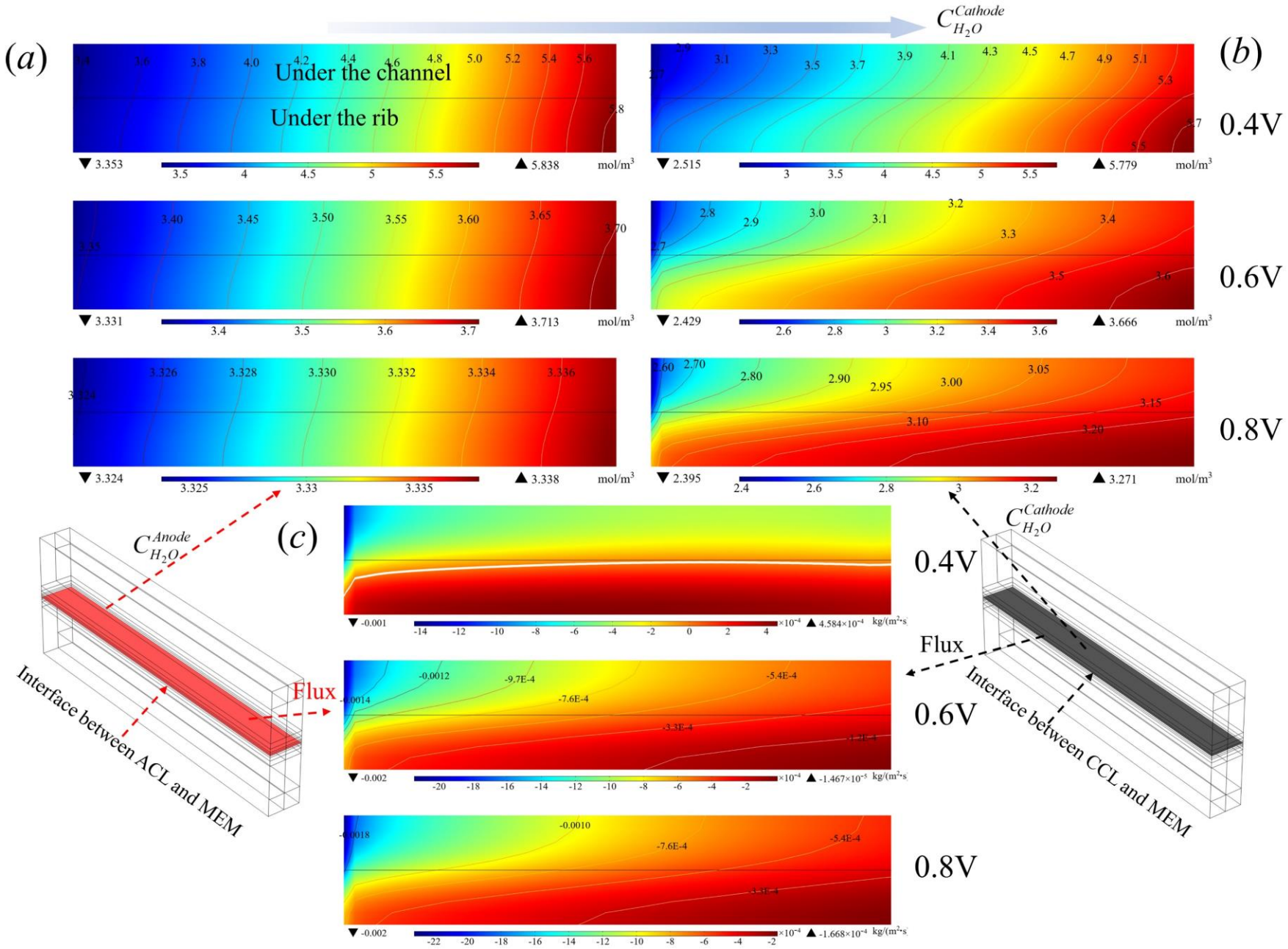

Fig. 7 Distribution of water vapor concentration and transport flux distribution at the interface between the catalyst layer and the membrane with RH of 60%. (a) Water vapor concentration distribution of anode, (b) Water vapor concentration distribution of cathode, (c) Distribution of water vapor transport flux between cathode and anode.

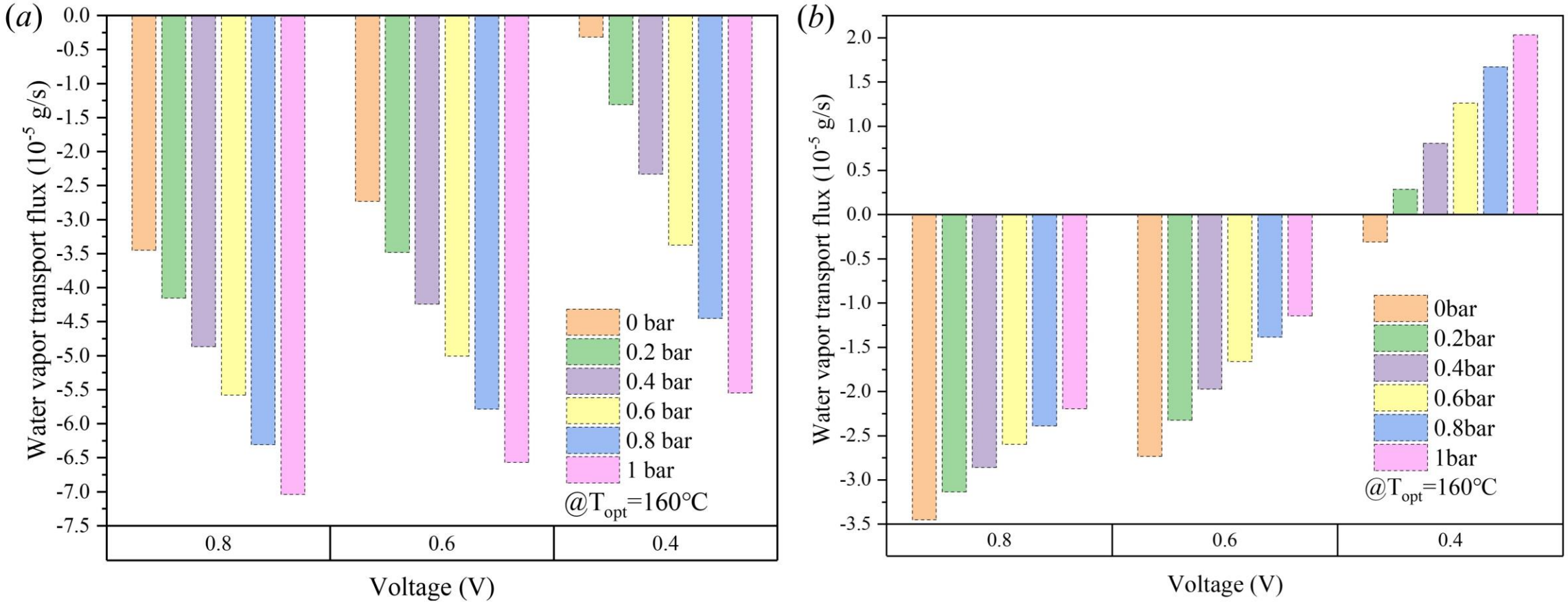

Fig. 8 Effect of the pressure difference between anode and cathode on the water vapor transport flux with RH of hydrogen is 60% at 60 ℃. (a) The anode pressure is higher than the cathode pressure, (b) The cathode pressure is higher than the anode pressure.

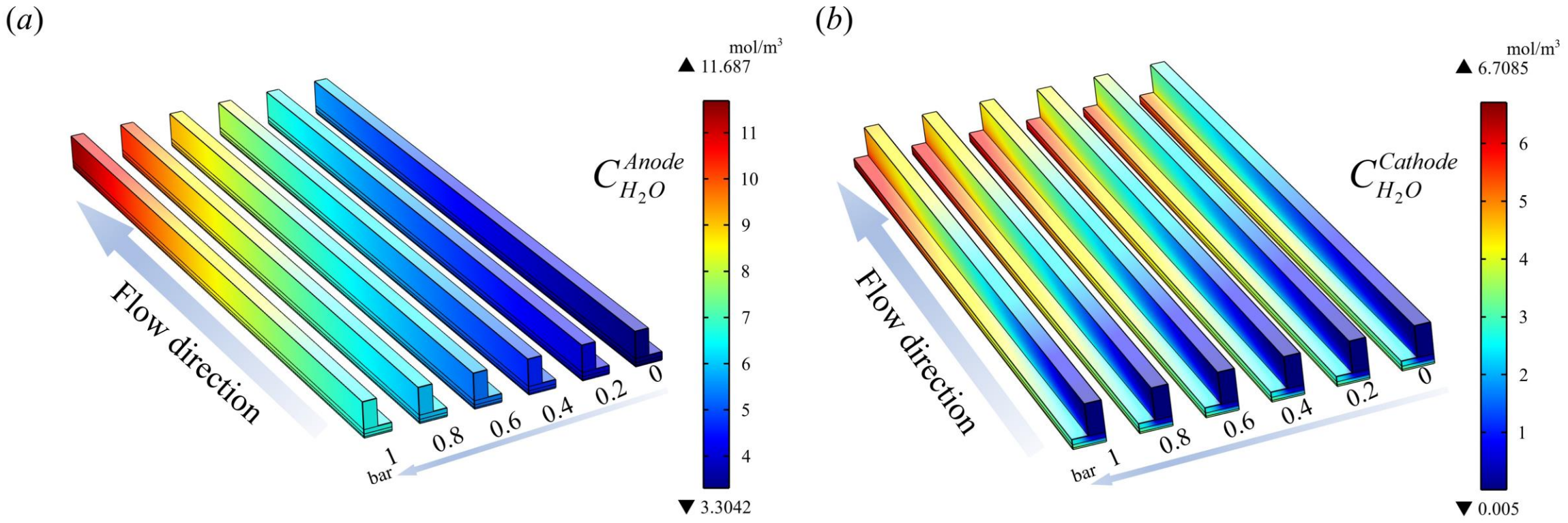

Fig. 9 Effect of the pressure difference between anode and cathode on the water vapor concentration at 0.4V with RH of hydrogen is 60% at 60 ℃. (a) Anode, (b) Cathode.

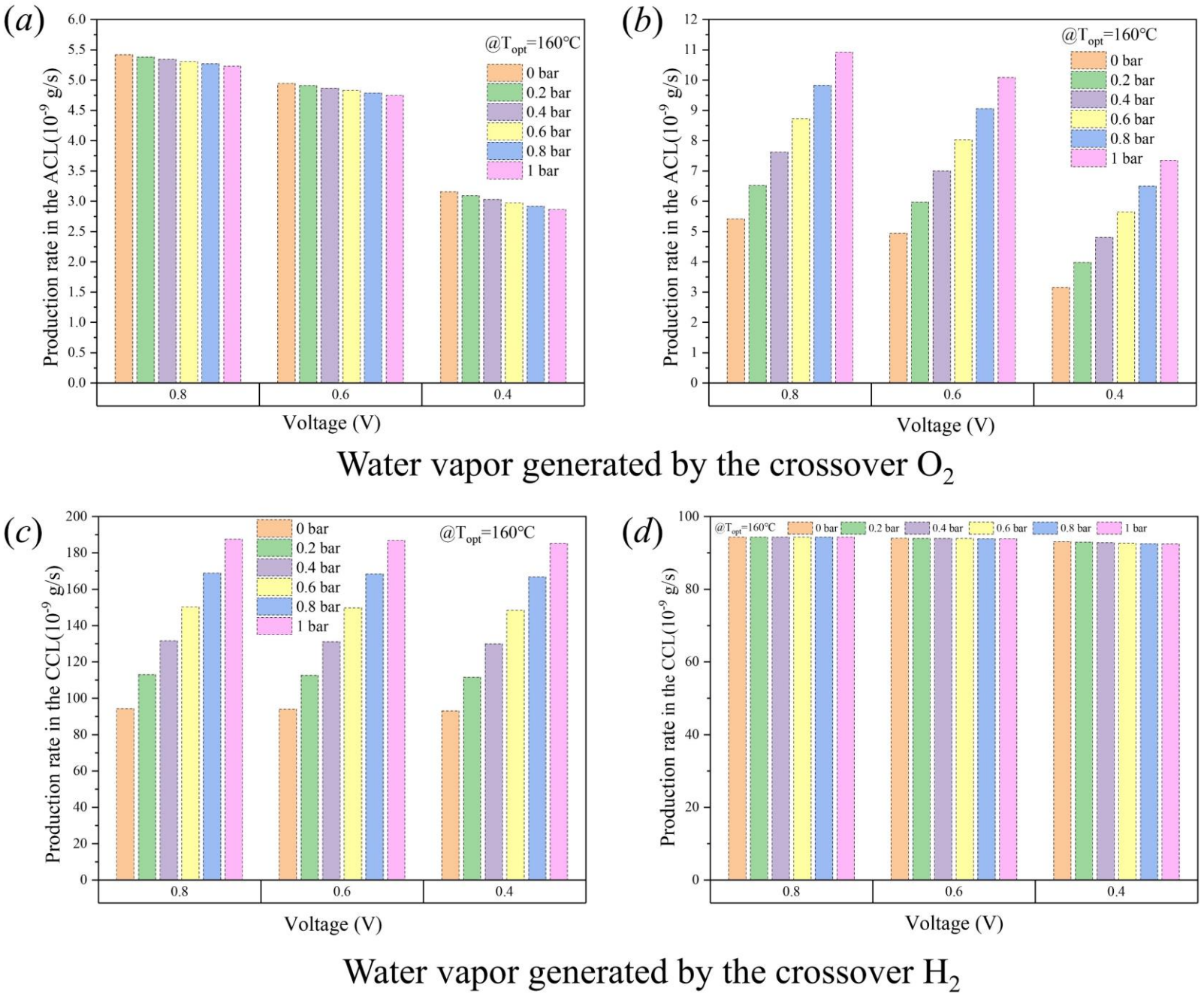

Fig. 10 Effect of the pressure difference between anode and cathode on the water vapor generated caused by crossover H_2 and O_2 in ACL and CCL. (a) and (c) Anode pressure is higher than cathode pressure, (b) and (d) Anode pressure is lower than cathode pressure.

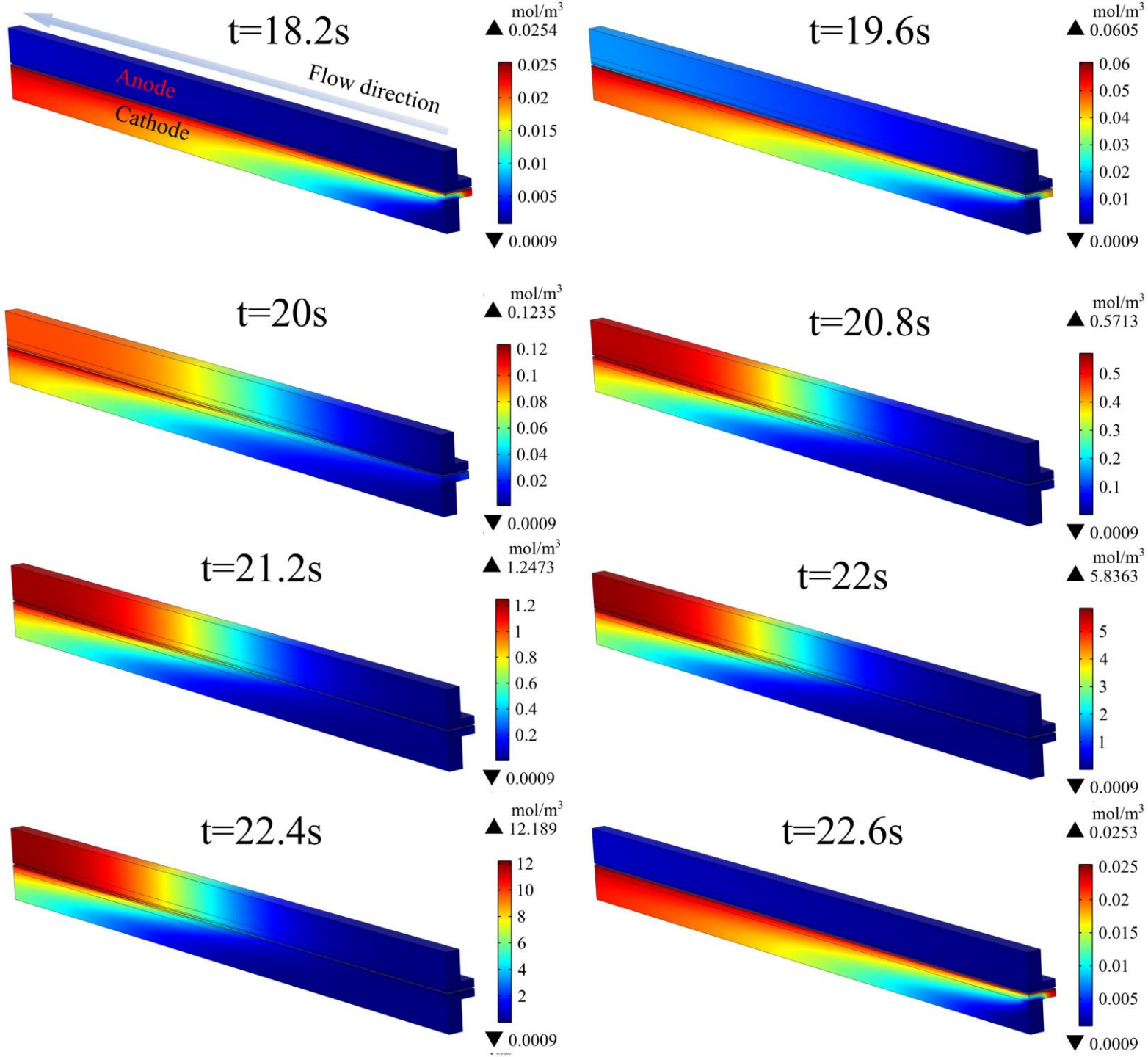

Fig. 11 The variation of water vapor concentration distribution in a purge cycle (18.2s-22.6s).

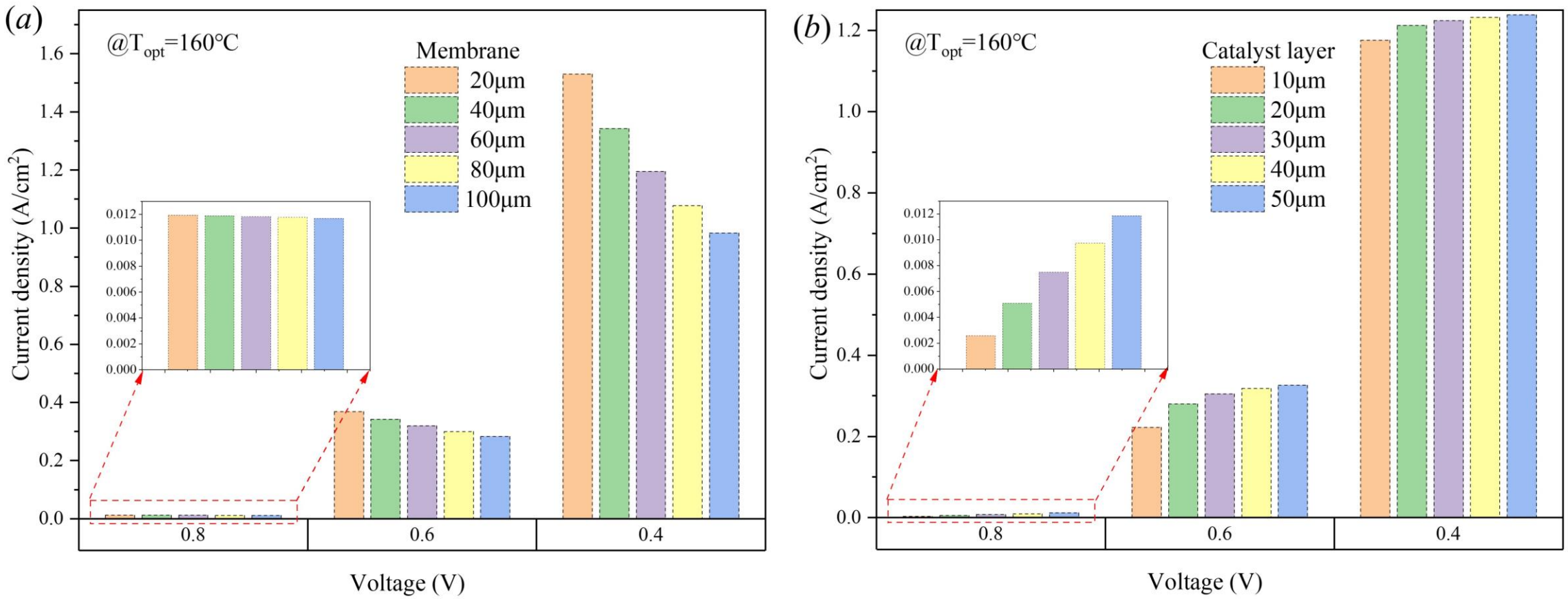

Fig. S1 Effect of PBI membrane thickness and catalyst layer thickness on the performance of HT-PEMFC. (a) PBI membrane, (b) Catalyst layer.

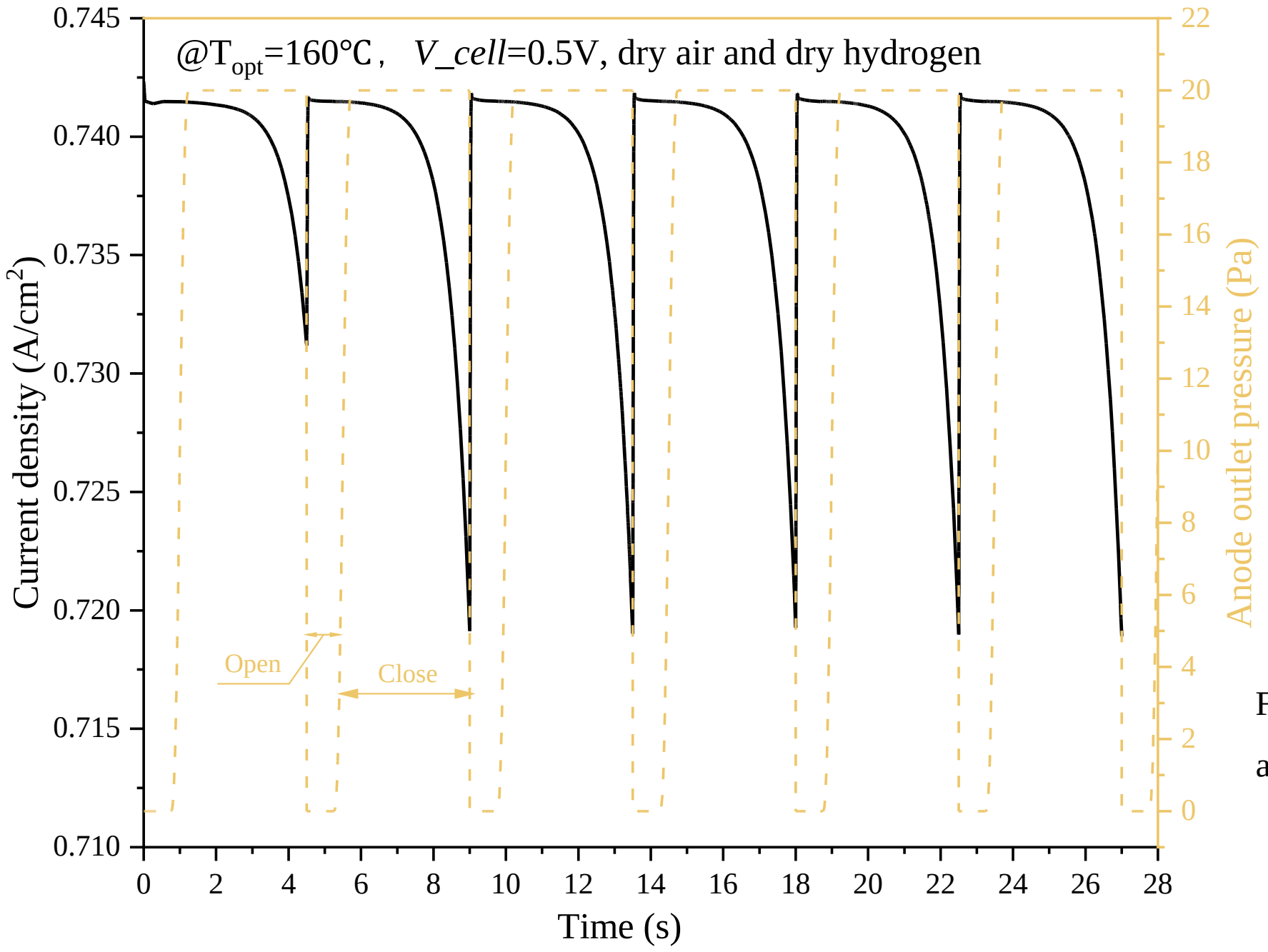

Fig. S2 The pressure setting of the anode outlet and the change of the output current with time.